Materials Today Bio 30 (2025) 101392

Contents lists available at ScienceDirect

Materials Today Bio

journal homepage: www.journals.elsevier.com/materials-today-bio

Construction and high-throughput screening of gradient nanowire coatings on titanium surface towards ameliorated osseointegration

Ruiyue Hang [a], Yuyu Zhao [a], Huanming Chen [a], Xiaomei Li [e], Runhua Yao [a], Yonghua Sun [a], Xiaohong Yao [a,**], Long Bai [c,***], Huaiyu Wang [d], Yong Han [b,****], Ruiqiang Hang [a,b,*]

[a] Shanxi Key Laboratory of Biomedical Metal Materials, College of Materials Science and Engineering, Taiyuan University of Technology, Taiyuan, 030024, China
[b] State-Key Laboratory for Mechanical Behavior of Materials, Xi'an Jiaotong University, Xi'an, 710049, China
[c] Institute of Translational Medicine, Shanghai University, Shanghai, 200444, China
[d] Center for Human Tissues and Organs Degeneration, Shenzhen Institute of Advanced Technology, Chinese Academy of Sciences, Shenzhen, 518055, China
[e] Shanxi Provincial Key Laboratory of Protein Structure Determination, Shanxi Academy of Advanced Research and Innovation, Taiyuan, 030012, China

ARTICLE INFO

Keywords:
High-throughput screening
Titanium implant
Gradient nanowire coating
Osseointegration

ABSTRACT

Surface nano-modification has emerged as an effective strategy to enhance osseointegration of titanium (Ti) implants. Despite its promise, rational optimization of surface nanomorphology for ameliorated osseointegration remains a significant challenge. Our research pioneering developed a one-step alkali etching technique to produce a gradient nanowire coating with continuously varied dimensions on Ti surfaces, which was subsequently served as a versatile platform for high-throughput screening of optimal dimensions to enhance osseointegration. The results showed that macrophages (MΦs) that mainly governed the initial inflammatory reaction exhibited a polarization tendency towards pro-healing M2 phenotype with decreased nanowire dimension due to nanomorphology-mediated focal adhesion formation and activation of its downstream signaling pathways (typically PI3K-Akt). Simultaneously, small-sized nanowires with diameter of 5.63–14.25 nm and inter-spacing of 29.42–57.97 nm were conductive to angiogenesis of endothelial cells (ECs) and osteogenesis of bone marrow mesenchymal stem cells (BMSCs), which may share similar mechanisms of MΦs. The *in vivo* results well corroborated these *in vitro* observations. The knowledge gained from the present work not only advance our understanding of the interaction between surface morphology and cells, but also potentially pave the way for efficient and cost-effective design of advanced biomaterial surfaces for better osseointegration.

1. Introduction

As the aging of global population, the incidence of oral and orthopedic diseases and the need for prosthetic surgeries have been on the rise [1,2]. Titanium (Ti) implants, prized for their exceptional mechanical properties, corrosion resistance, and biocompatibility, have been favored in prosthetic replacements [3]. Nevertheless, implant failure usually occurs predominantly due to their poor osseointegration ability [4]. Osseointegration is a complex and dynamic process that unfolds over time and involves various cell types, mainly including macrophages (MΦs), endothelial cells (ECs), bone marrow stem cells (BMSCs), and osteoblasts/osteoclasts [5], which govern inflammatory reaction, angiogenesis, osteogenesis and bone reconstruction phases of osseointegration, respectively. Surface modification is a powerful approach to endow Ti implants with favorable osseointegration ability [6]. However, current researches predominantly target single-cell functions, neglecting exploration of the surface-mediated collective behavior of multiple cell types and their synergistic interactions. Deeper insights into these interactions are crucial for advancing the design of more bioactive Ti implants, thereby improving clinical outcomes and patient well-being [7].

Nano-morphological modifications of implant surfaces have

* Corresponding author. Shanxi Key Laboratory of Biomedical Metal Materials, College of Materials Science and Engineering, Taiyuan University of Technology, Taiyuan, 030024, China.
** Corresponding author.
*** Corresponding author.
**** Corresponding author.
E-mail addresses: xhyao@tyut.edu.cn (X. Yao), bailong@shu.edu.cn (L. Bai), yonghan@mail.xjtu.edu.cn (Y. Han), hangruiqiang@tyut.edu.cn (R. Hang).

https://doi.org/10.1016/j.mtbio.2024.101392
Received 16 October 2024; Received in revised form 2 December 2024; Accepted 6 December 2024
Available online 7 December 2024

garnered significant attention in recent years for their inherent advantages in promoting osseointegration, owing to their exceptional biocompatibility and ability to modulate inflammation [8,9]. Our previous study focused on preparing TiO_2 nanotubes of varying diameters on the surface of Ti implants, revealing that nanotubes with a 15 nm diameter, as opposed to 60 nm and 120 nm, markedly down-regulated inflammation during the early stages of osseointegration [10]. Similarly, a research has demonstrated that a 85 nm nanorod spacing exhibited superior coordination of osteogenic differentiation both *in vitro* and *in vivo* compared to that of 45 nm spacing [11]. Additionally, nanorods with a 75 nm spacing enhanced the phenotypic transition of M1 to M2 MΦs, along with promoting angiogenesis and osteogenesis, in contrast to spacings of 40 nm, 140 nm, and 245 nm [12]. Despite these findings, existing studies often employ discrete nanoscale dimensions, potentially overlooking the optimal nanostructure dimensions or shapes. This may result in an obscured understanding of how nanostructure size influences the functions of cells involved in osseointegration. Moreover, the validation of continuous nanostructures necessitates the preparation of a large number of specimens, which is both time-consuming and labor-intensive, and may not facilitate optimal nanoscale screening. Therefore, there is an urgent need to adopt a new research paradigm to overcome the limitations of the traditional trial-and-error approach, enabling efficient material preparation and breaking the barrier of discontinuity in preparation parameters.

Recent advancements in high-throughput material preparation techniques have made it feasible to achieve controllable gradient composition on implant surface [13]. The solvent evaporation method has demonstrated success in the high-throughput preparation of antimicrobial peptides on Ti surfaces, offering a novel approach for optimizing peptide density and screening [14]. Compared with gradient composition, the construction of gradient topologies on Ti surfaces is another important paradigm for the rational design and preparation of biofunctionalized surfaces. Generating microarrays provided solutions for evaluating a wide range of cellular parameters [15]. However, there remains a lack of comprehensive investigation into the construction of gradient nanomorphology on the surface of Ti implants. To address the concern, we firstly developed a time-sequential microdroplet technique to etch Ti surfaces with NaOH solution, yielding progressively increasing diameters and inter-spacings of Na_2TiO_3 nanowires (Scheme 1). Next, we conducted high-throughput screening using key effector cells involved in osseointegration (MΦs, ECs, and BMSCs) on the gradient nanowire coatings. Subsequently, two specific nanowire sizes were

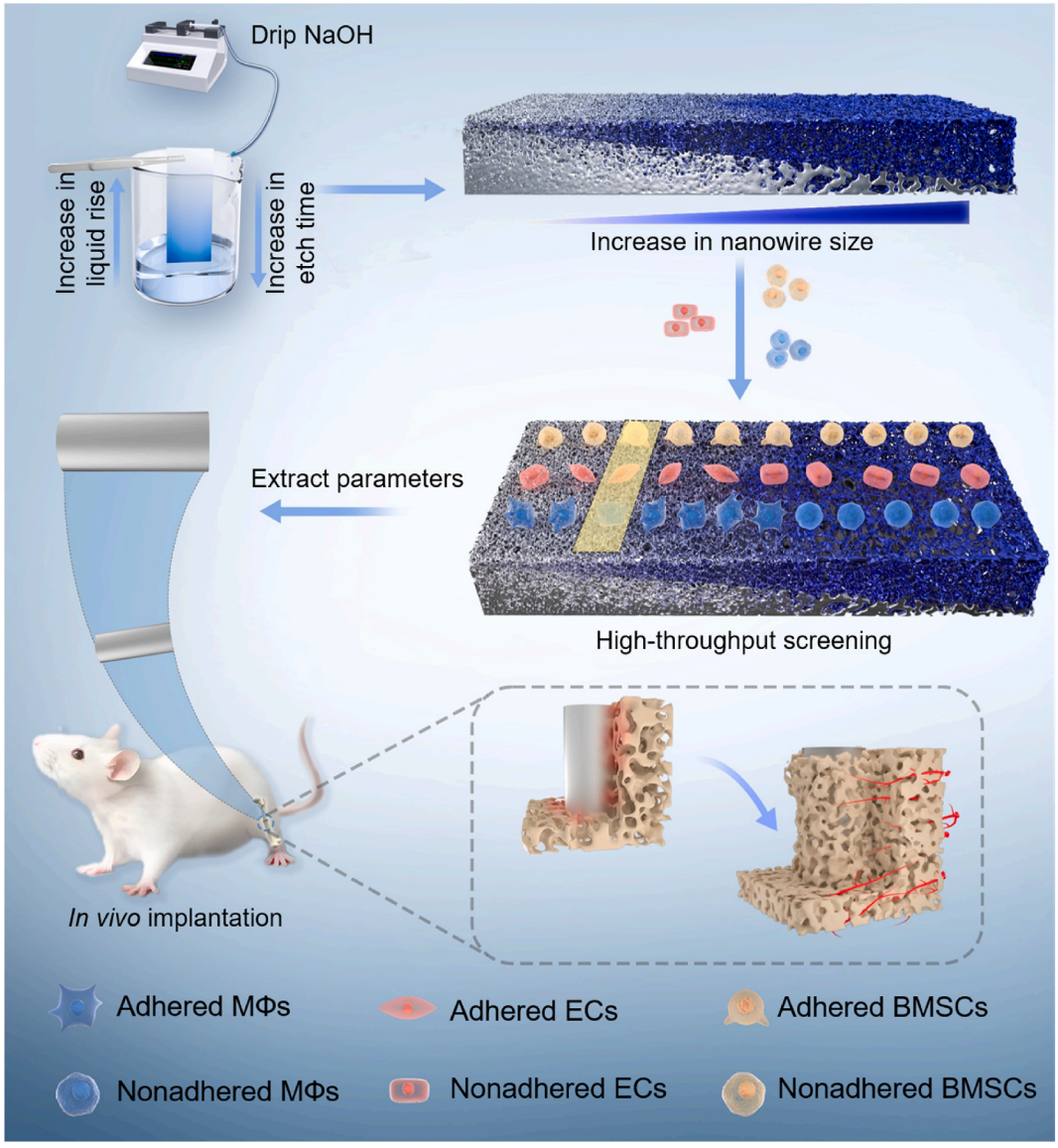

Scheme 1. Schematic representation of preparation and high-throughput screening of gradient nanowire coating with excellent osteointegration ability.

selected based on the screening results, and the effects of the screened nanowire coatings on the immunomodulation of MΦs and the underlying mechanisms were investigated. Finally, the *in vitro* results were validated by *in vivo* experiments. The present work not only developed a novel technique to fabricate gradient nanowire coating on Ti, but also demonstrated the feasibility to realize high-throughput screening of multicellular functions by using the coating, which may be of great value for better and efficient surface design of Ti and other types of biomaterials.

2. Materials and methods

2.1. Specimen preparation

Commercial Ti plates (99.6 % purity) with dimension of 32 mm × 10 mm × 1.5 mm were used as substrates. The Ti substrates were sequentially ultrasonic cleaned in acetone, absolute ethyl alcohol, and deionized water for 20 min sequentially, followed by air drying. Subsequently, the Ti plates were etched in a water solution comprising HF (40 %, Sinopharm, China), HNO_3 (65 %, Sinopharm, China), and deionized water (in a 1:1:2 vol ratio) for 10 s to remove surface oxide film, which were designated as T. The T specimens were positioned vertically in a 100 mL beaker. Next, 2.5 M, 5 M, 10 M, or 15 M NaOH (Tianjin Damao, China) solution was slowly (0.5 mL/h) introduced into the beaker using a syringe pump at room temperature. After 96 h of injection, the specimens were ultrasonically cleaned with deionized water for 5 min and then air dried.

2.2. Specimen characterization

The surface and cross-sectional morphologies of the specimens was analyzed by field-emission scanning electron microscope (FE-SEM, Gemini SEM 300, Zeiss, Germany). The microstructures of the specimens were examined using high-resolution transmission electron microscopy (HR-TEM, JEM-2100F, JEOL, Japan) equipped with selected area electron diffraction (SAED). The surface chemical compositions and chemical states for the elements of interest were measured by X-ray photoelectron spectroscopy (XPS, K-alpha, Thermo Fisher, USA). The surface wettability was characterized with a pendant drop method on a contact angle analyzer (JC2000DF, Powereach, China).

2.3. Cell culture

The murine-derived macrophage cell line RAW 264.7 (MΦ, Catalog number: TCM13) and human umbilical vein endothelial cell line EA. hy926 (EC, Catalog number: GNHu39) were obtained from the Cell Bank of Chinese Academy of Sciences (Shanghai, China). Bone marrow stem cells (BMSCs) were isolated from the tibias and femurs of a 4-week-old rat under sterile conditions, and only 3 to 5 passages of BMSCs were used for the follow-up experiments. MΦs and ECs were cultured in high-glucose Dulbecco's modified eagle medium (DMEM, Gibco, USA) supplemented with 10 % fetal bovine serum (FBS, BI, China), 200 units/mL penicillin (Aladdin, China), 200 μg/mL streptomycin (Aladdin, China), and 1.5 mg/mL sodium bicarbonate ($NaHCO_3$, Sinopharm, China). BMSCs were cultured in Minimum Essential Medium Alpha Medium (α-MEM, Gibco, USA) containing 10 % FBS, 100 units/mL penicillin, 100 μg/mL streptomycin, and 2.2 mg/mL $NaHCO_3$ at 37 °C under a humidified atmosphere of 5 % CO_2. For osteogenic induction differentiation, the BMSCs were cultured with osteogenic induction medium (complete culture medium supplemented with 10 mM β-glycerophosphate (Sinopharm, China), 50 μg/mL ascorbic acid (Sinopharm, China), and 1 mM dexamethasone (Sinopharm, China)) after 2 days of culturing in normal medium. All kinds of culture media were refreshed every other day.

2.4. Immune responses of MΦs cultured on the gradient coatings

2.4.1. MΦ morphology

To observe the morphology of MΦs cultured on the gradient coating surface, the cells were seeded on the gradient coatings at a density of 2 × 10^4 cells/cm^2 in 6-well plates for 1 day. To activate the MΦs, lipopolysaccharide (LPS, 100 ng/mL, Beyotime, China) was added to the culture medium and incubated for 6 h. Then the serum-free medium was added into the well, followed by incubation for another 12 h. Subsequently, the cells were rinsed three times with PBS, fixed with 2.5 % glutaraldehyde at 4 °C for 40 min, and sequentially dehydrated through graded ethanol concentrations of 50 %, 60 %, 70 %, 80 %, 90 %, 95 %, and 100 % (v/v) for 10 min. After sputtered coated with a thin platinum layer, the cell morphology was observed on the FE-SEM.

2.4.2. Immunofluorescence staining of iNOS and CD206

MΦ phenotype cultured on the gradient coatings was evaluated by immunofluorescence staining. Briefly, MΦs were seeded onto the gradient coatings at a density of 5 × 10^4 cells/cm^2 in 6-well plates, stimulated with LPS as aforementioned, and subsequently incubated for another 12 h. After being rinsed thrice with PBS at 4 °C, MΦs were fixed with 4 % paraformaldehyde (PFA, pH = 7.2, Phygene, China) for 30 min, followed by rinsing with PBS for three times. The MΦs were then permeabilized by Saponin (Beyotime, China) for 20 min and blocked by immunostaining block solution (Quick Block, Beyotime, China) for 1 h to prevent antibodies from binding to unwanted proteins. After incubated with hybrid primary antibody (iNOS, 1:2000, Abcam, UK; CD206, 1:2000, Abcam, UK) at 4 °C for 12 h, the cells on the gradient coatings were then incubated with hybrid secondary antibodies (Goat Anti-Mouse IgG H&L (Alexa Fluor® 488, Abcam, UK), 1:1000; Goat Anti-Rabbit IgG H&L (Alexa Fluor® 555, Abcam, UK), 1:1000) at room temperature for 1.5 h. After that, the nuclei were counterstained with DAPI for 5 min. Finally, the images were captured by confocal laser scanning microscope (CLSM, C2Plus, Nikon, Japan) after being rinsed with PBS. The mean fluorescence intensity (MFI) of iNOS and CD206 was quantified by the NIH ImageJ 1.45 software.

2.5. Biological responses of ECs cultured on the gradient coatings

2.5.1. EC morphology

The ECs were seeded on the gradient coatings at a density of 1 × 10^4 cells/cm^2 in 6-well plates and cultured for 1 day. Next, the cells were rinsed three times with PBS, fixed with 2.5 % glutaraldehyde at 4 °C for 40 min, and sequentially dehydrated through graded ethanol concentrations of 50 %, 60 %, 70 %, 80 %, 90 %, 95 %, and 100 % (v/v) for 10 min. After sputtered coated with a thin platinum layer, the cell morphology was observed on the FE-SEM. The area of SEM images for individual cells was quantified using Digimizer software.

2.5.2. Cytotoxicity and cytoskeleton assembly

Cytotoxicity was evaluated by Live/Dead viability/cytotoxicity kit for mammalian cells (Invitrogen, USA) according to the manufacturer's instructions. Briefly, ECs were seeded on the gradient coatings at a density of 1 × 10^4 cells/cm^2 in 6-well plates and cultured for 1, 3, and 5 days. After rinsing the specimens with PBS for three times, 150 μL working solution in the kit was added onto the specimen surface. After incubated for 40 min in darkness, the specimens were rinsed with sterile PBS again and observed by the CLSM. The number and the MFI of images was quantified using ImageJ 1.45 software.

The ECs were seeded on the gradient coatings at a density of 1 × 10^4 cells/cm^2 in 6-well plates and cultured for 1 day. After rinsing three times with sterile PBS and fixed with 4 % PFA for 30 min, the cells on the gradient coatings were stained with fluorescein isothiocyanate (FITC)-Phalloidin (Invitrogen, USA) for 40 min and counterstained with 4, 6-diamidino-2-phenylindole (DAPI, Beyotime, China) for 5 min. Finally, the fluorescence images of the cytoskeleton were captured with the

CLSM.

2.5.3. Nitric oxide production

The intracellular nitric oxide (NO) levels were evaluated using a NO fluorescence probe 4-amino-5-methylamino-2′, 7′-difluorofluorescein, diacetate (DAF-FM DA, Beyotime, China) according to instructions provided by the manufacturer. After being cultured on the gradient coatings at a density of 1×10^4 cells/cm^2 in 6-well plates for 2 days, the ECs were rinsed three times with PBS and incubated with 50 μL of 5 mM DAF-FM DA for 20 min. Finally, the cells were rinsed three times with PBS and observed on the CLSM. The MFI of the NO was calculated by the NIH ImageJ 1.45 software.

2.5.4. Immunofluorescence staining of CD31

The expression levels of CD31 in ECs were evaluated by immunofluorescence staining. Briefly, ECs were seeded on the gradient coatings at a density of 1×10^4 cells/cm^2 in 6-well plates and cultured for 2 days. Then, ECs were rinsed three times with PBS, fixed with 4 % PFA for 30 min, and immediately rinsed with PBS to remove excess PFA. Subsequently, ECs were blocked by immunostaining block solution (Quick Block™, Beyotime, China) for 1 h to prevent antibodies from binding to unwanted proteins, followed by incubation with primary antibody (CD31, 1:2000, Abcam, UK) at 4 °C for 12 h. Next, ECs were rinsed with PBS and incubated with secondary antibodies (1:100, m-IgGκ BP-CFL 488, Santa Cruz Biotechnology, USA) for 1.5 h. After that, the nuclei were counterstained with DAPI for 5 min. Finally, the ECs were observed by the CLSM after being rinsed by PBS. The MFI of CD31 was calculated by the NIH ImageJ 1.45 software.

2.6. Biological responses of BMSCs cultured on the gradient coatings

2.6.1. BMSC morphology

BMSCs were seeded on the gradient coatings at a density of 1×10^4 cells/cm^2 in 6-well plates and cultured for 1 day. The following experimental details were the same as that in Section 2.5.1.

2.6.2. Cytotoxicity and cytoskeleton assembly

The BMSCs were seeded on the gradient coatings at a density of 1×10^4 cells/cm^2 in 6-well plates and cultured for 1, 3, and 5 days. The following experimental details to evaluate cytotoxicity were the same as that in Section 2.5.2. The BMSCs were seeded at the gradient coatings at a density of 1×10^4 cells/cm^2 in 6-well plates and cultured for 1 day. The following experimental details to observe cytoskeleton were the same as that in Section 2.5.2.

2.6.3. ALP activity

After being seeded on the gradient coatings at a density of 1×10^4 cells/cm^2 in 6-well plates and cultured in normal medium for 2 days, the BMSCs were osteogenic induced in the osteogenic induction medium for 3 and 7 days. At each time point, the BMSCs were rinsed three times with sterile PBS and fixed with 4 % PFA for 30 min. Then, the cells were incubated with working solution in BCIP/NBT Alkaline Phosphatase Color Development Kit (Beyotime, China) at 4 °C for 12 h. Finally, the images were captured on a stereoscopic microscope (SMZ745T, NIKON, Japan).

2.6.4. Collagen secretion

The secretion of type I collagen by BMSCs was quantified by Direct Red 80 (Sigma-Aldrich, USA) staining. After 2 days of culturing in the normal medium with a seeding density of 1×10^4 cells/cm^2 in 6-well plates, the cells were osteogenic induced for 7 and 14 days. At each time point, the cells were rinsed three times with sterile PBS and fixed by 4 % PFA for 30 min, followed by staining with 0.1 % solution of Direct Red 80 in aqueous saturated picric acid for 18 h. After being rinsed with 0.1 M acetic acid and dried in the air, the images were captured by the stereoscopic microscope.

2.6.5. ECM mineralization

The ECM mineralization of BMSCs was evaluated by Alizarin Red S (Sigma-Aldrich, USA) staining. After 2 days of culturing in a normal medium with a seeding density of 1×10^4 cells/cm^2 in 6-well plates, the cells were osteogenic induced for 14 and 21 days. At each time point, the cells were fixed with 75 % ethanol for 1 h, rinsed three times with sterile PBS, and stained with 40 mM Alizarin Red S (pH = 4.2) for 30 min. After rinsing with distilled water, the images were captured by the stereoscopic microscope.

2.7. Angiogenetic functionality of ECs stimulated by conditioned DMEM

2.7.1. Extraction of specimen preparation parameters and preparation of conditioned DMEM

Based on the biological responses of the three types of cells cultured on the surface of gradient coatings, we extracted typical parameters to prepare non-gradient coatings. MΦs were seeded on the above specimens at a density of 5×10^4 cells/cm^2 in 6-well plates for 24 h. After activated by LPS and cultured in serum-free medium as aforementioned, the resultant culture medium was collected as the conditioned medium of MΦs. ECs were cultured in the conditioned DMEM (mixture of fresh DMEM and conditioned medium of MΦs in the volume ratio of 1:1) in the following experiments.

2.7.2. Nitric oxide production

After ECs (at a density of 1×10^4 cells/cm^2) were seeded in the 24-well plates for 1 day with normal medium and 2 days with conditioned DMEM. NO production of ECs was evaluated as the preceding methods in Section 2.5.3.

2.7.3. Immunofluorescence staining of CD31

After ECs (at a density of 1×10^4 cells/cm^2) were seeded on the 24-well plates for 1 day with normal medium and 2 days with conditioned DMEM. CD31 level of ECs was evaluated as the methods described in Section 2.5.4.

2.7.4. Migration of ECs

To investigate the activity of EC migration stimulated by conditioned DMEM, the cells were seeded in 24-well plates at a density of 4×10^4 cells/cm^2 and cultured in a normal medium for 1 day. After ECs were incubated in conditioned DMEM for 2 days to reach confluence, the cell-free gaps were made by 200 μL tips on the bottom of the culture plates. Next, each well was rinsed three time with PBS to remove non-adhered cells and cell debris and incubated for 6, 12, and 18 h. At each time point, the ECs were observed with an inverted microscope (ECLIPSE Ts2R-FL, Nikon, Japan). Digimizer software was used to quantify the migration distance.

2.7.5. In vitro angiogenesis

The *in vitro* angiogenesis assay of ECs was conducted using ECMatrix™ (Catalog number: ECM625, Millipore, America). The ECMatrix™ gel was placed into each well of 96-well plate and the ECs were seeded on the gel at a density of 6×10^4 cells per well. Subsequently, the ECs were incubated with conditioned DMEM from various specimens at 37 °C for 12 h and 24 h. At each time point, cell images were captured using the inverted microscope, and Photoshop CC software was employed to quantify the number of branch points (nodes), mesh-like circles (circles), and tube-like parallel cell lines (tubes) formed by the ECs.

2.8. Osteogenic functionality of BMSCs stimulated by conditioned α-MEM

BMSCs were cultured with conditioned α-MEM to assess MΦ-mediated osteogenesis. If not otherwise specified in the following experiments, BMSCs were seeded in 24-well cell culture plates, cultured in conditioned α-MEM (the ratio of α-MEM and the conditioned medium of

MΦs was 1:1 (v/v)), and induced in conditioned osteogenic induction medium supplemented with 50 % conditioned medium of MΦs for inducing osteogenic differentiation.

2.8.1. ALP activity

After being seeded in 24-well cell plates at a density of 1×10^4 cells/cm^2 and cultured in normal medium for 2 days, the BMSCs were cultured in conditioned osteogenic induction culture medium for 3 and 7 days. The ALP activity of BMSCs was evaluated as the preceding methods in Section 2.6.3.

2.8.2. Collagen secretion

After 2 days of culture in normal medium and subsequent osteogenic induction for 7 and 14 days, secretion level of type I collagen of BMSCs was assessed as described in Section 2.6.4. For the quantitative assay, the stain was eluted with 1 mL of the fading solution (0.2 M NaOH/methanol 1:1 (v/v)) for 30 min. The absorbance of the resultant solution was measured on a microplate reader (Infinite F50, TECAN, Switzerland) at a wavelength of 570 nm.

2.8.3. ECM mineralization

After 2 days of culture in normal medium and subsequent osteogenic induction for 14 and 21 days, ECM mineralization of BMSCs was assessed as described in Section 2.6.5. For the quantitative analysis, 500 μL 10 % cetylpyridinium chloride (MREDA, China) in 10 mM sodium phosphate (Xiya, China) was used to dissolve the dye. The absorbance of the resultant solution was measured on the microplate reader at a wavelength of 570 nm.

2.9. mRNA sequencing and data analysis

MΦs were seeded on the screened specimens in 6-well plates at a density of 10×10^4 cells/cm^2. After activated by LPS and cultured in serum-free medium as aforementioned, the MΦs were lysed by TRIZOL (Sigma-Aldrich, USA) and then the lysates were collected for sequencing. The gene expression profiles were accessed through the sequencing platform of BGI-500 of Beijing Genomic Institution (BGI, Shenzhen, China). To guarantee the sequencing saturation and gene mapping distribution, quality control was undertaken. The Fragments per Kilobase of transcript per Million mapped reads (FPKM) value was used to express relative gene abundance and standardized read count data. The Pearson correlation coefficient $|r| > 0.9$ was used to evaluate the stability and sensitivity of gene expression to ensure the consistency of gene transcription in the different groups.

In this work, the differently expressed genes (DEGs) were indicated by $\log_2$ fold change (FC) $> |1|$ and p-value <0.001. The Venn diagram was applied to show the overall distribution of DEGs. The comprehensive expression tendency of DEGs in different groups were exhibited in hierarchical clustering heatmaps. Based on the gene ontology (GO) and Kyoto Encyclopedia of Genes and Genomes (KEGG) database (p-value <0.001 as the threshold), the biological implications, cellular functional processes, and significant signaling pathways of DEGs were analyzed. Protein-protein interaction (PPI) networks obtained by the STRING database and visualized by Cytoscape 3.8.2 were utilized to exhibit interaction network structures among DEGs with special trends.

2.10. In vivo evaluation of osseointegration

2.10.1. Surgical procedure

The animal experiments were approved by Ethics Committee of Academic Committee of Taiyuan University of Technology (No. TYUT2023070501). Cylindrical specimens (Φ1.5 × 3 mm) were prepared based on optimized parameters for *in vivo* implantation experiments in rat tibia. Female rats weighing around 350 g were used for animal testing. The rats were performed with general anesthesia by intramuscular injections of 1 % pentobarbital at a dose of 30 mg/kg body weight. A 1.5 mm diameter circular hole was drilled in the platform with a surgical electronic drill and thoroughly rinsed with saline to remove bone fragments. Six rod specimens of each group were randomly implanted into the tibias of six different rats and each tibia of a rat was implanted with one rod specimen. After the specimens were randomly implanted into the bone cavities, the musculature and skin of the surgical sites were carefully sutured in layers. All surgical procedures were performed under aseptic conditions. At the time points of 3 days, 7 days and 6 weeks, the bilateral tibias containing cylindrical implants were obtained from the sacrificed rats and fixed in 4 % PFA.

2.10.2. Western blot

Western blot analysis was performed to assess inflammatory reaction near the interface of implant and bone. Cylindrical implants with a 1 cm bone length were harvested after 3 and 7 days of surgery. Next, the bones were finely sheared into pieces, placed in a grinder, and ground with 1.2 mL of radioimmunoprecipitation assay (RIPA) buffer (Beyotime, China) containing a cocktail of protease and phosphatase inhibitors (Thermo Fisher Scientific) for 30 min on ice. Subsequently, the mixture was centrifuged at 12,000 rpm for 20 min at 4 °C. The supernatants were then gathered after centrifugation. Protein concentration was determined using the bicinchoninic acid (BCA) protein assay kit (Beyotime, China). Specimens with a protein concentration of 3 μg/μL were mixed with 5 × SDS loading buffer (Beyotime, China) at a 4:1 ratio and heated for 10 min at 100 °C to facilitate protein denaturation. 20 μL protein was separated by sodium dodecyl sulfate polyacrylamide gel electrophoresis (SDS-PAGE) and transferred to a poly (vinylidene fluoride) (PVDF) membrane. Then the membrane was blocked by QuickBlock™ Western (P0252 Beyotime, China) for 1 h at room temperature and incubated with primary antibodies: anti-iNOS (ab178945, Abcam, UK), anti-IL-1β (ab254360, Abcam, UK), anti-CD206 (ab64693, Abcam, UK), anti-Arg1 (ab239731, Abcam, UK), anti-Ang1 (ab183701, Abcam, UK), anti-CD31 (ab9498, Abcam, UK), anti-OPN (sc-21742, Santa Cruz Biotechnology, USA), anti-ALP (sc-271431, Santa Cruz Biotechnology, USA) and anti-GAPDH (sc-365062, Santa Cruz Biotechnology, USA) overnight at 4 °C, followed by incubated with HRP (horseradish peroxidase) conjugated secondary antibodies Goat Anti-Mouse IgG H&L (ab6789, Abcam, UK) and Goat Anti-Rabbit IgG H&L (ab6721, Abcam, UK) for 2 h. Autoradiograms were obtained using an ECL western blotting substrate (BeyoECL Star, Beyotime, China) and captured by chemiluminescence imager (Tanon-5200, China).

2.10.3. X-ray imaging

X-ray imaging was performed immediately after the procedure to observe the implantation in each group. The rats lay flat on the platform, and the implants were observed and captured using a Digital photographic X-ray machine (SD5.0A, Wanke, China).

2.10.4. Micro-computed tomography analysis

To evaluate the newly formed bone around the implants, the tibias containing cylindrical implants were harvested and imaged by micro-computed tomography (micro-CT, SkyScan1275, SkyScan Company, Germany). A hollow cylinder with a thickness of 100 μm distally from the implant surface was defined as the volume of interest (VOI) for analysis and the 3D images were constructed by SCANCO evaluation software. The percentages of bone volume to total volume (BV/TV), trabecular thickness (Tb.Th), trabecular number (Tb.N), trabecular separation (Tb.Sp), were calculated as measurements of new bone mass and its distribution. And the new bone formation area and bone-implant contact (BIC) were also calculated for detecting implant osseointegration.

2.10.5. Histological evaluation

After scanning by Micro-CT, the fixed tibia implants were dehydrated in the graded ethanol, embedded in polymethylmethacrylate and cut into longitudinal sections with a thickness of 50 μm. The sections

were then stained with toluidine blue for histological analysis. The images were captured by the stereoscopic microscope.

2.11. Statistical analysis

All experiments were repeated at least three times and the specimens were prepared in triplicate. The quantitative data were presented in the form of mean ± standard deviation. Statistical analysis was implemented with the Statistical Package for Social Sciences version 14 (SPSS v14.0, IBM, USA) software. Values of $p < 0.05$, $p < 0.01$ and $p < 0.001$ indicated statistical difference, significant statistical difference, and extremely significant statistical difference, respectively.

3. Results

3.1. Specimen characterization

Firstly, we investigated the impact of NaOH concentration on the

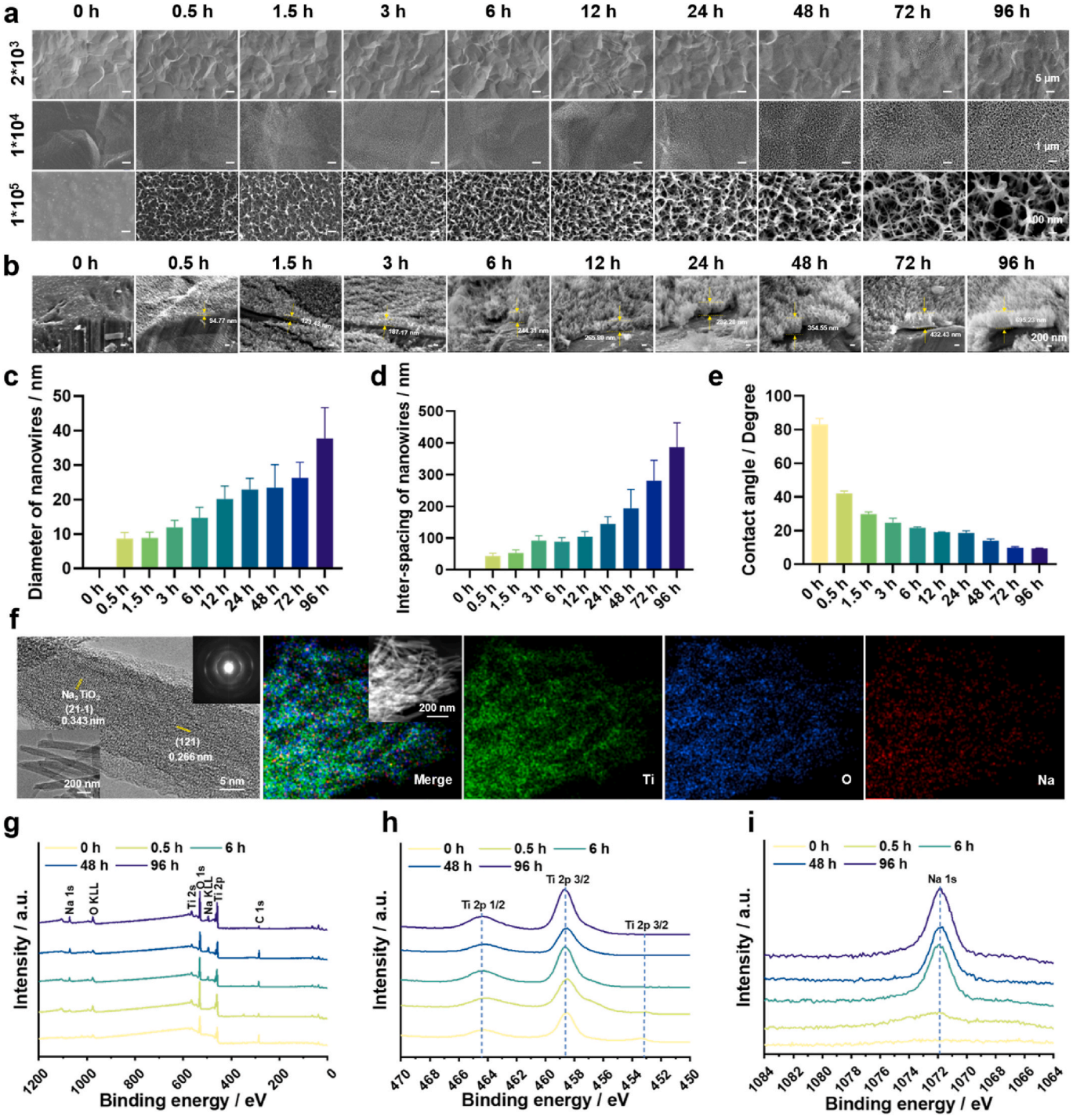

Fig. 1. Physicochemical characterization of the gradient coatings. (a) Surface SEM morphology of the gradient coatings prepared in 2.5 M of NaOH. (b) SEM images of the specimen cross-sections. (c) Diameter of the nanowires. (d) Inter-spacing of the nanowires. (e) Contact angles of the gradient coatings. (f) TEM and EDS mapping images of the gradient coatings. (g) XPS survey spectra of the gradient coatings. (h) High-resolution XPS spectra of Ti 2p. (i) High-resolution XPS spectra of Na 1s.

surface morphology of Ti. Our previous work has shown that concentrations of NaOH below 2.5 M and above 15 M were unable to produce nanostructures on Ti surfaces [16]. Therefore, 2.5 M, 5 M, 10 M and 15 M of NaOH were selected in the present work. The macroscopic morphology of the gradient coating shows the surface transitioned from blue to gray as the time progress of alkaline etching (Fig. S1). The microscopic morphology of the gradient coatings is shown in Fig. 1a and Fig. S2a, b and c. Low-magnification images reveal that micro-pits of 10–15 μm in size appeared on all the specimen surfaces. Middle-magnification images show that evenly distributed nanowires could be grown on all the specimen surfaces. However, apparent cracks could be observed on the surfaces of specimens fabricated in 10 M of NaOH with prolonged etching time (Fig. S2b). This effect became more pronounced with higher concentrations (Fig. S2c), indicating an earlier onset of structural collapse. High-magnification images disclose the nanowire diameter and inter-spacing increased with time for all the groups, showing apparent gradient features. The thickness of the surface nanowire coating increased gradually with alkaline etching time (Fig. 1b). The diameter and inter-spacing of nanowires increased from 8.7 nm to 43.2 nm at 0.5 h to 37.7 nm and 386.2 nm at 96 h for etching in 2.5 M of NaOH, respectively (Fig. 1c and d). They ranged from 14.1 nm to 30.9 nm–39.4 nm and 153.5 nm for 5 M of NaOH, from 18.8 nm to 60.4 nm–41.5 nm and 103.7 nm for 10 M of NaOH, and from 8.1 nm to 19.1 nm–60.1 nm and 140.2 nm for 15 M of NaOH, respectively (Figs. S2d–i). Collectively, the coating fabricated in 2.5 M of NaOH had evenly distributed nanowires, and the largest range of nanowire diameters and inter-spacings. Therefore, the 2.5 M group was used in subsequent experiments. The contact angle of the 2.5 M group decreased as the increases of alkali etching time (Fig. 1e), indicating enhanced surface hydrophilicity. TEM and elemental mapping images (Fig. 1f) confirmed the nanowire was composed of Na_2TiO_3. XPS analysis of the gradient coating revealed the presence of Ti, O, and C elements at the 0 h of location, while Na 1s peak emerged after etching for 0.5 h and 96 h (Fig. 1g and h). The 96 h of location exhibited an intensive Na 1s peak, indicating high Na content due to prolonged etching (Fig. 1 i).

3.2. The effects of gradient coating on immune response of MΦs

The morphology of MΦs cultured on the surface of specimen is depicted in Fig. 2a. Low-magnification images revealed a uniform distribution of MΦs on the surface, indicating favorable support for MΦ attachment and growth by these surface structures. High-magnification images showed that MΦs cultured on the 0 h of location appeared spherical with minimal pseudopods, whereas those cultured on alkaline-etched sites such as 0.5 h, 1.5 h, and 3 h exhibited a fusiform or elliptical shape, accompanied by abundant lamellipodia and filopodia. Notably, MΦs at the 0.5 h of location displayed a larger surface area and a smoother fusiform shape with increased lamellipodia compared to those at 1.5 h and 3 h. At the 6 h of location, the interaction between pseudopods and the substrate gradually weakened, leading to a decrease in the number of pseudopods. By 72 h and 96 h, pseudopods were nearly absent.

To investigate if the gradient coating influences MΦs polarization, immunofluorescence staining was performed. iNOS is a typical M1 marker found in the cytoplasm, while CD206 acts as a M2 marker expressed on the cell surface [17–19]. Fig. 2b displayed the fluorescence

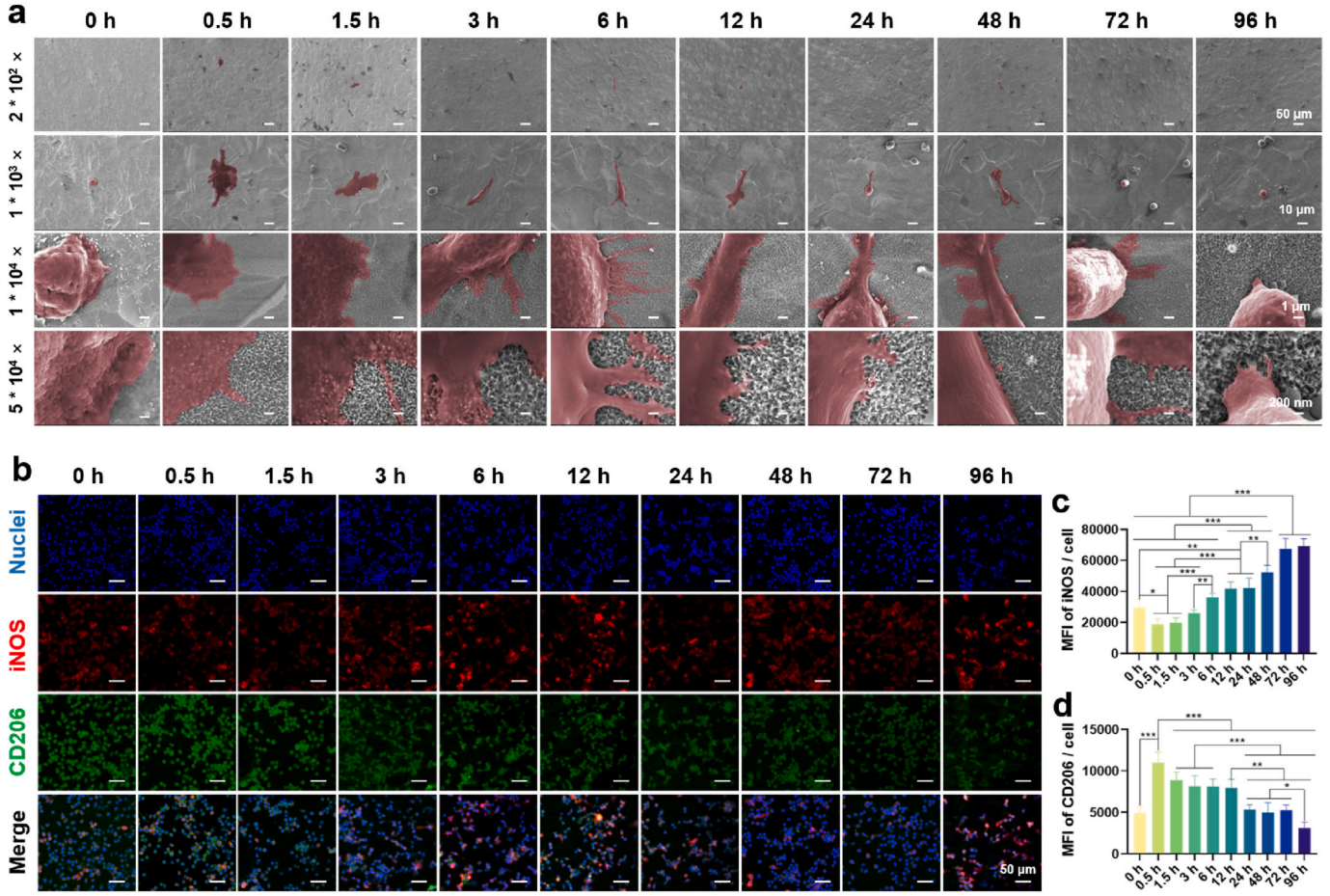

Fig. 2. Immune response of MΦs cultured on the gradient coating. (a) Morphology of MΦs after cultured on the coating surface for 24 h. (b) Immunofluorescence images of M1 phenotype marker iNOS (red) and M2 phenotype marker CD206 (green) of the MΦs after cultured on the coating surface for 24 h. (c) The fluorescence intensity of iNOS. (d) The fluorescence intensity of CD206. $n = 3$, $^{*}p < 0.05$, $^{**}p < 0.01$, and $^{***}p$ using one-way ANOVA with a Tukey post hoc test.

images of iNOS and CD206. The iNOS (in red) at 0.5 h and 1.5 h of locations exhibited a lower intensity compared with 0 h and other locations. As the increase of etching time, fluorescence intensity of iNOS increased accordingly, while that of CD206 (in green) showed an opposite trend. Quantitative results (Fig. 2c and d) corroborated the qualitative observations, suggesting that the nanowires with small dimensions tended to polarize MΦs towards M2 phenotype, while those with large dimensions to M1 phenotype.

3.3. The effects of gradient coating on angiogenesis of ECs

Angiogenesis near the bone-implant interface is recognized as a prerequisite for osseointegration [20]. In this study, ECs were cultured on the gradient coating to assess angiogenic activity. The morphology of ECs is shown in Fig. 3a. Low-magnification images showed the cells distributed on the specimen surface evenly. Medium-magnification images showed that ECs gradually changed from a polygonal shape to a spiked shape and their spreading area decreased as the increase of alkali etching time. High-magnification images showed that ECs at the 0.5 h of location exhibited enhanced surface adherence and adopted a polygonal shape, suggesting that small nanowires effectively promoted cell adhesion. The quantitative data of SEM images also verified the above results (Fig. S3). The fluorescence images of cytoskeleton assembly (Fig. 3b) showed that the ECs at 0.5 h–12 h of locations exhibited well-organized stressed-fibers, while that at 24 h–96 h of locations were poorly organized. Fig. 3c presented the fluorescence images of live/dead staining of ECs. Dead cells (in red) could not be observed and cell number increased with time for all the groups. Quantitative results of cell number (Fig. 3d) indicated that the cells cultured on the location between 0.5 and 12 h underwent notable proliferation, while that on the 24–96 h was slow. MFI of single cell cultured on the gradient coating also showed obvious difference (Fig. 3e). Increase of nanowire dimension reduced cell viability. These results clearly indicate the nanowires with small size can simultaneously promote cell proliferation and viability.

NO is a typical vasoactive mediator and sufficient NO can enhance adhesion and proliferation of ECs [21]. Fig. 4a and b depicted the impact of the gradient coating on NO generation of ECs. The cells at the 0.5 h of location exhibited higher NO expression compared to that of 0 h and other locations, as indicated by high fluorescence intensity. CD31 is the most abundant constitutive co-signal receptor glycoprotein on ECs and can regulate the response to biomechanical stimuli by binding to most endothelial receptors involved in mechanoreception [22]. Fig. 4c and d presented the CD31 expression of ECs. Consistently, ECs cultured on the 0.5 h of location highly expressed CD31 when compared with that at 0 h and other locations. With increasing nanowire size, the MFI decreased steadily, with pronounced drop observed at 72 h and 96 h of locations.

3.4. The effects of gradient coating on osteogenesis of BMSCs

Osteogenesis is imperative throughout the process of osseointegration. The implant surface morphology regulates the osteogenic activity of BMSCs, ultimately determining the fate of the implant [23]. We firstly evaluated the initial adhesion and spreading behaviors of BMSCs (Fig. 5a), which are prerequisites for later proliferation and differentiation [24]. Low-magnification images revealed an even distribution of BMSCs on the surface, indicating robust BMSC adhesion. Middle-magnification images showed that BMSCs on the surfaces with small-sized nanowires area (0.5 h, 1.5 h, 3 h, and 6 h) exhibited polygonal appearance with large spreading area. In contrast, the cells on large-sized nanowires area (48 h, 72 h, and 96 h) showed round appearance with small spreading area. This is also verified by the quantitative data (Fig. S4). High-magnification images revealed the pseudopodia of BMSCs in close contact with small-sized nanowires area when compared with that of large-sized ones, indicating they can offer abundant adhesion sites. Fluorescence images of cytoskeleton (Fig. 5b) revealed significant cell spreading with well-organized F-actin at 0 h, 0.5 h, 1.5 h, 3 h, and 6 h of locations, outperforming later time intervals. Particularly, BMSCs at the 0.5 h of location exhibited expansive spreading areas characterized by F-actin fibers encompassing the entire cell, along with distinct lamellipodia and filopodia protruding from cell peripheries. Live/dead staining showed there were no dead (in red) cells in all the locations of the specimen at any time point (Fig. 5c). BMSCs show a decreasing trend in quantity and viability from the 0.5 h of location with small nanowires to the 96 h of location with large nanowires (Fig. 5d and e), indicating that the larger nanowires inhibit BMSC proliferation.

Alkaline phosphatase (ALP) activity, collagen secretion, and extracellular matrix (ECM) mineralization are indicative markers of early, middle, and later stages of osteogenic differentiation, respectively. ALP activity staining images (Fig. 6a) revealed significantly enhanced ALP expression in BMSCs at the 0.5 h of location after 3 days of osteogenic induction, surpassing other locations. Prolonging alkali etching time reduced ALP expression levels, which persisted and became more pronounced after 7 days of induction. Qualitative results of collagen secretion and ECM mineralization (Fig. 6b and c) were consistent with ALP activity. After 7, 14 and 21 days of induction, BMSCs at the 0.5 h of location exhibited superior collagen secretion and calcium deposition when compared with other locations.

3.5. Effects of immune microenvironment generated by MΦs on angiogenesis and osteogenesis

The initial immune response could promote the recruitment of ECs and BMSCs to the surface of the implant [25]. The signals that control the recruitment of ECs and BMSCs include the chemokines CCL2, CXCL8 and SDF-1, all of which can be secreted by MΦs [26–28]. As an essential process of osseointegration, the newly formed vessels can transport oxygen, nutrients and growth factors to the BMSCs [12,29]. Osteogenesis is the last part of the osseointegration, which determines the level of new bone mass on the implant surface [30]. Based on the immune response of MΦs to the gradient coating, unetched Ti, and the Ti etched for 0.5 h and 48 h were selected and fabricated to explore their effects on MΦ-mediated immunomodulation in relation to angiogenesis and osteogenesis. These three groups of specimens were denoted as T, TA-0.5, and TA-48, respectively. Among them, the nanowire diameters of TA-0.5 and TA-48 range from 5.63 to 14.25 nm and 12.31–42.72 nm, respectively. The nanowire inter-spacing ranges from 29.42 to 57.67 nm and 97.45–339.94 nm, respectively. Next, the conditioned media of MΦs cultured on the three groups of specimens were collected to investigate the influence of the immune microenvironment on ECs and BMSCs.

The influences of immune microenvironment created by polarized MΦs on angiogenesis of ECs are presented in Fig. 7. The qualitative (Fig. 7a) and quantitative (Fig. 7b) results of the cell migration showed all the ECs underwent migration with time, and TA-0.5 group possessed the strongest migration ability when compared with other two groups. Fig. 7c shows CD31 fluorescence images of ECs. The TA-0.5 group exhibited the highest fluorescence intensity and there was no significant difference between T and TA-48 groups. The quantitative result (Fig. 7d) is consistent with the qualitative images. The influence of the conditioned DMEM on the production of NO was assessed (Fig. 7e and f). There was no obvious difference between T and TA-48 groups, while the TA-0.5 group can synthesize the most NO. To investigate the angiogenetic functionality, ECs were cultured on the matrix gels in the conditioned DMEM for 6 h and 12 h. Optical images (Fig. 7g) show that the points, circles and tubes were formed in all the groups and their number decreased with time. The quantitative results (Fig. 7h and i) are consistent with the qualitative images. The ECs in TA-0.5 group showed the best ability of angiogenesis. In summary, these results indicate that the immune microenvironment produced by MΦs cultured on small-sized nanowires is more favorable for angiogenesis.

Fig. 8 depicts the modulation of BMSC osteogenesis by the immune

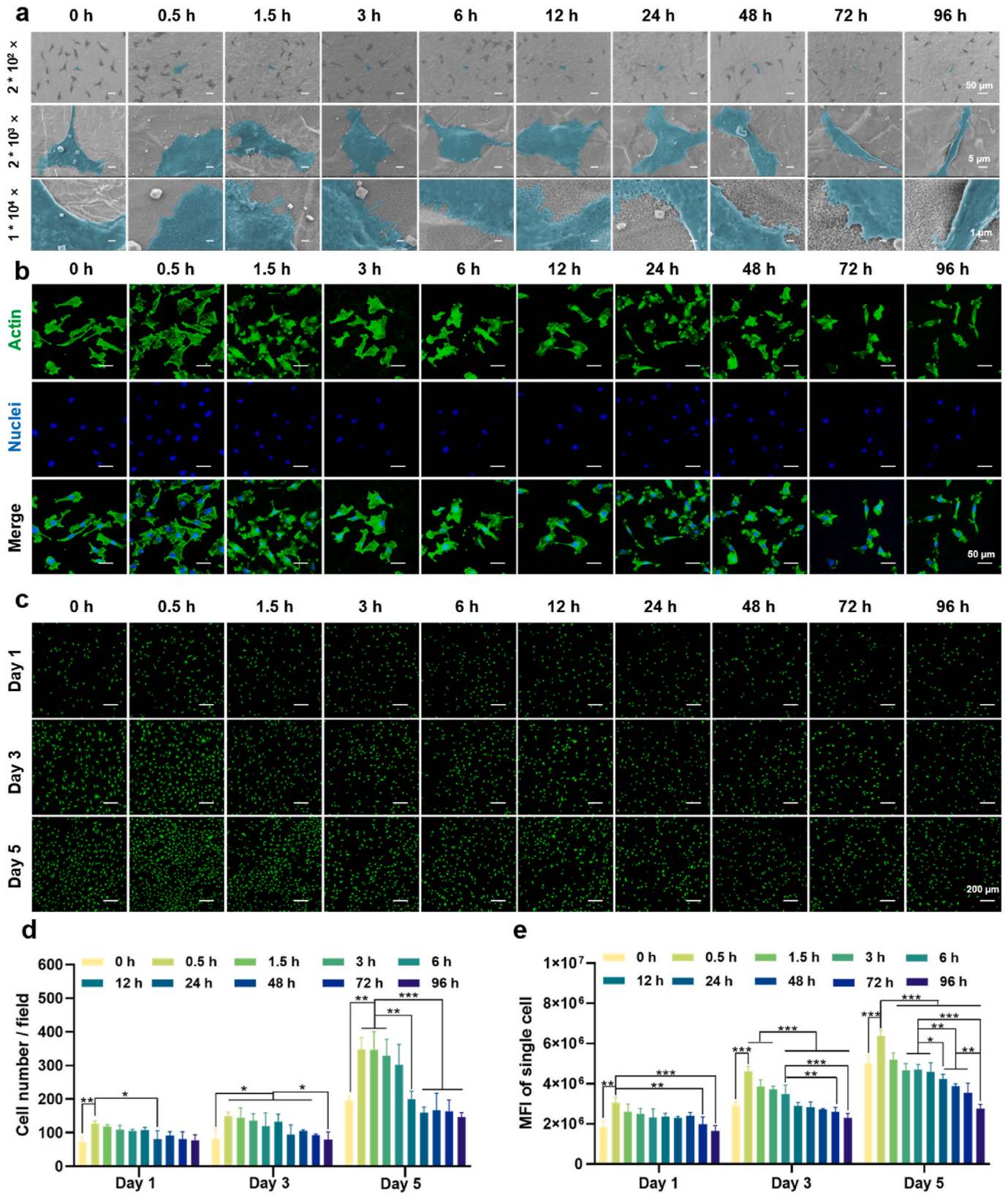

Fig. 3. Morphology, cytoskeleton assembly, and viability of ECs cultured on the gradient coating. (a) Morphology of ECs after cultured on the coating surface for 24 h. (b) Fluorescence images of cytoskeleton of ECs after cultured on the coating surface for 24 h. (c) Fluorescence images of live/dead staining of ECs after cultured on the coating surface for 1, 3 and 5 days. (d) Number of the ECs. (e) Mean fluorescence intensity of the EC. $^{*}p < 0.05$, $^{**}p < 0.01$, and $^{***}p < 0.001$ using one-way ANOVA with a Tukey post hoc test.

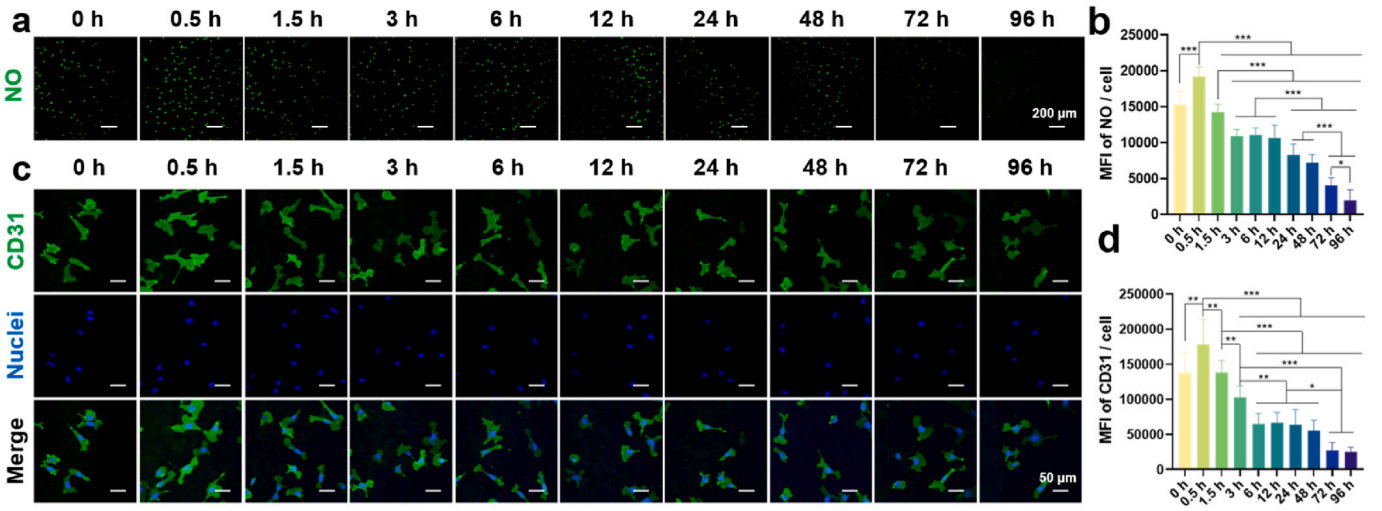

Fig. 4. Angiogenic activity of ECs cultured on the gradient coating. (a) Fluorescence images of NO of ECs after cultured on the coating surface for 24 h. (b) The quantitative results of the NO. (c) Fluorescence images of CD31 of ECs after cultured on the coating surface for 24 h. (d) The quantitative results of the CD31. $n = 3$, $^{*}p < 0.05$, $^{**}p < 0.01$, and $^{***}p < 0.001$ using one-way ANOVA with a Tukey post hoc test.

microenvironment created by MΦs. Osteogenesis of BMSCs in conditioned α-MEM was assessed via ALP activity, collagen secretion, and ECM mineralization. Qualitative optical images of ALP staining (Fig. 8a) revealed enhanced deep blue NBT-formazan with prolonged induction time, particularly prominent in the TA-0.5 group, indicating high ALP activity elicited by conditioned α-MEM from TA-0.5 compared to other groups. The results of collagen secretion (Fig. 8b) and ECM mineralization (Fig. 8c) of BMSCs were consistent with ALP activity. Quantitative results (Fig. 8d and e) confirmed these findings. This could be due to TA-0.5 prompted polarization of MΦs into the M2 phenotype, which possessed the ability to generate a pro-osteo-genic immune microenvironment by secreting cytokines such as TGF-β1. Binding of exogenous TGF-β1 to the BMSCs receptor TGF-β1R phosphorylates SMAD [31] and subsequently activates Runx2, which directly promotes the expression of osteogenesis-related genes such as OCN [32], COL1 [33], and ALP [34].

3.6. *mRNA sequencing of MΦs cultured on different specimen surfaces*

To investigate the potential mechanisms of nanowire coating-mediated immune responses of MΦs, mRNA sequencing analysis of MΦs cultured on T, TA-0.5 and TA-48 was applied. The Pearson correlation coefficients and Venn plot among the groups of the specimens are shown in Fig. S5 and Fig. S6. The value between each group was greater than 0.98, confirming the stability of gene expression and repeatability of the experiments. Venn diagram displayed the quantitative DEGs among T, TA-0.5 and TA-48 (Fig. 9a). A total of 1152 genes were T *vs* TA-0.5 specific DEGs, 505 genes were T *vs* TA-48 specific DEGs and 114 genes were TA-0.5 *vs* TA-48 specific DEGs. A pairwise comparison was implemented to identify the expression profile among the groups. 1040 genes were upregulated and 1005 genes were downregulated of TA-0.5 when compared with T (Fig. 9a). Similarly, 771 genes were upregulated and 726 genes were downregulated of T when compared with TA-48 (Fig. 9e). 331 genes were upregulated and 189 genes were downregulated of TA-0.5 when compared with TA-48 (Fig. 9i).

Bioinformatic analysis of DEGs in T *vs* TA-0.5 was implemented to investigate the effects of the nanowires on the immune responses of MΦs. Then the GO functional enrichment analysis of DEGs was performed and all enriched functions were divided into three types: biological processes, molecular functions and cellular components and the top 20 are displayed in Fig. S7a. Go term enrichment analysis of T *vs* TA-0.5 indicated that the upregulated DEGs were concentrate in cell cycle, DNA replication, Focal adhesion, while the downregulated DEGs were enriched in the inflammatory response, immune system process and positive regulation of NF-κB transcription factor activity (Fig. S7d). The top 20 KEGG pathways were divided into upregulated pathways and downregulated pathways (Fig. 9b). The upregulated pathways were mainly gathered in the cell cycle, MAPK signaling pathway, focal adhesion signaling pathway and phosphoinositide 3-kinase (PI3K)-AKT signaling pathway, while the downregulated pathways were concentrated in TNF signaling pathway, p53 signaling pathway, NF-κB signaling pathway and Toll-like receptor signaling pathway. The genes involved in these pathways were further clustered to investigate the interactions at the protein level (Fig. 9c and d). There were abundant links directed to Cdk1, Pik1 and Rfc4 in the upregulated genes, while down-regulated genes were heavily linked to IL-1β, IL-6, TNF, Mmp9 and CCL2. Cdk1 is an important gene that drives cell division [35]. Cdk1 is activated and phosphorylated by B-type cell cycle proteins to regulate activities associated with mitotic progression and cytokinesis, such as cytoskeletal reorganization, mitotic spindle assembly and function, and cytokinesis [36]. Phosphorylation of Cdk1 contributes to the activation of the mitotic kinase PIK1, which in turn promotes cell proliferation [37]. Rfc4 is one of several subunits of the replication factor C complex and acts as a polymerase co-protein in DNA replication and repair [38]. It is a pleiotropic cytokine involved in host responses to microbial invasion, inflammation, immune regulation, metabolic responses, hematopoietic processes and tumor progression [39]. IL-1β affects important cellular functions such as reducing DNA content, decreasing protein synthesis and intracellular energy production, and inducing apoptosis and necrosis in beta cells [40,41]. As pro-inflammatory cytokines, IL-6 and TNF can be tested in acute and chronic inflammation [42,43]. Mmps are involved in many pathological processes and Mmp9 represents a marker of inflammation [44]. Chemokines are a superfamily of secreted proteins involved in immunomodulatory and inflammatory processes in which Ccl2 is a chemokine of inflammation [45].

Bioinformatic analysis of DEGs in T *vs* TA-48 was performed to investigate the large-sized nanowire on the immune responses of MΦs. As for GO term analysis of T *vs* TA-48, the upregulated DEGs were mainly concentrated in cell cycle, DNA repair and cell division, while the downregulated DEGs were mainly concentrated in the inflammatory response, apoptotic process, and cellular response to lipopolysaccharide (Figs. S7b and e). The top 20 KEGG pathways were divided into upregulated pathways and downregulated pathways (Fig. 9f). The upregulated pathways were enriched in focal adhesion, PI3K-AKT signaling pathway and DNA replication while the downregulated pathways were mainly concentrated in the NF-κB, TNF, IL-17, and Toll-like receptor

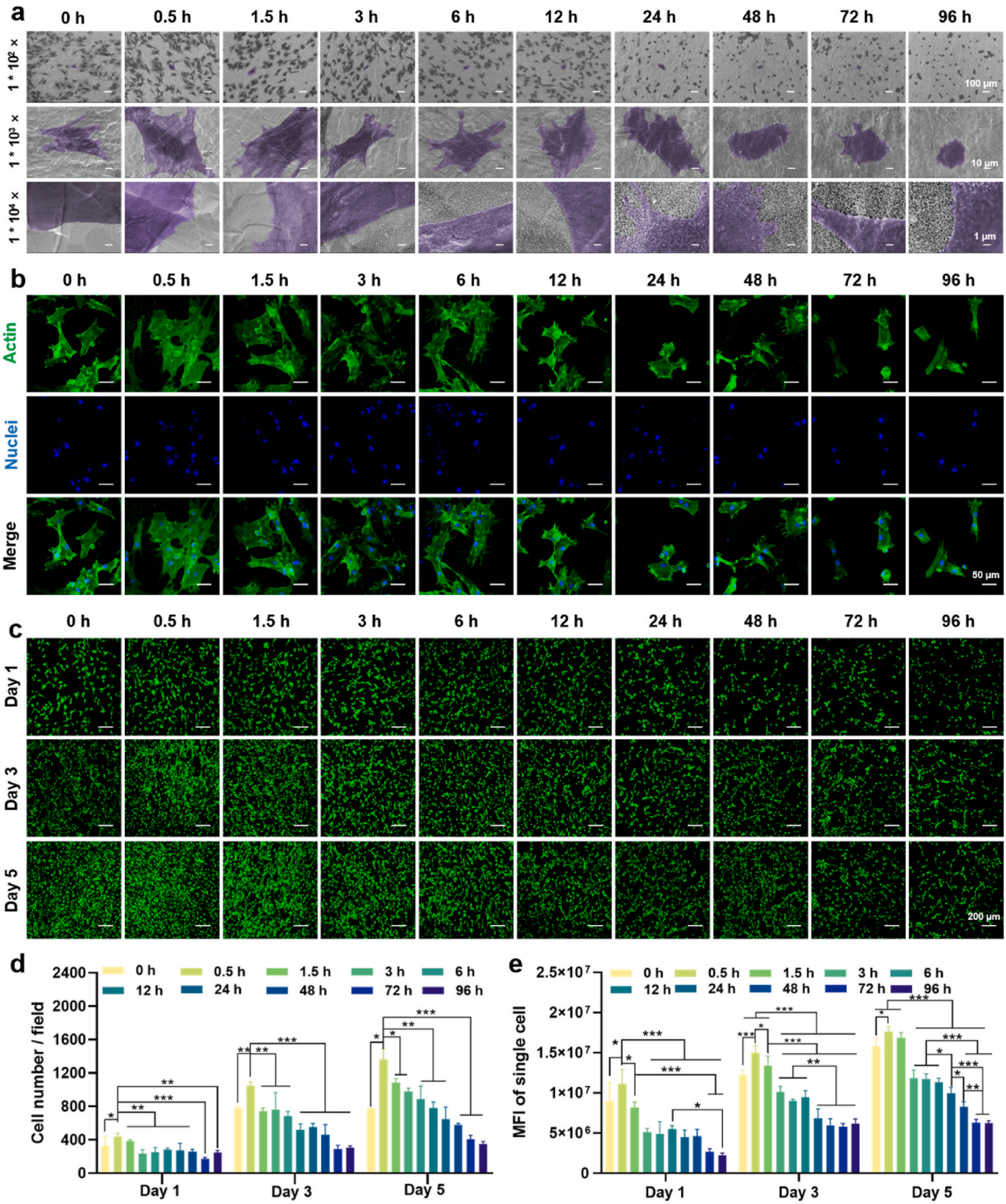

Fig. 5. Morphology, cytoskeleton assembly, and viability of BMSCs cultured on the gradient coating. (a) Morphology of BMSCs after cultured on the coating surface for 24 h. (b) Fluorescence images of cytoskeleton of BMSCs after cultured on the coating surface for 24 h. (c) Fluorescence images of live/dead staining of ECs after cultured on the coating surface for 1, 3 and 5 days. (d) Number of BMSCs counted by live/dead staining. (e) Mean fluorescence intensity of the BMSC. $^{*}p < 0.05$, $^{**}p < 0.01$, and $^{***}p < 0.001$ using one-way ANOVA with a Tukey post hoc test.

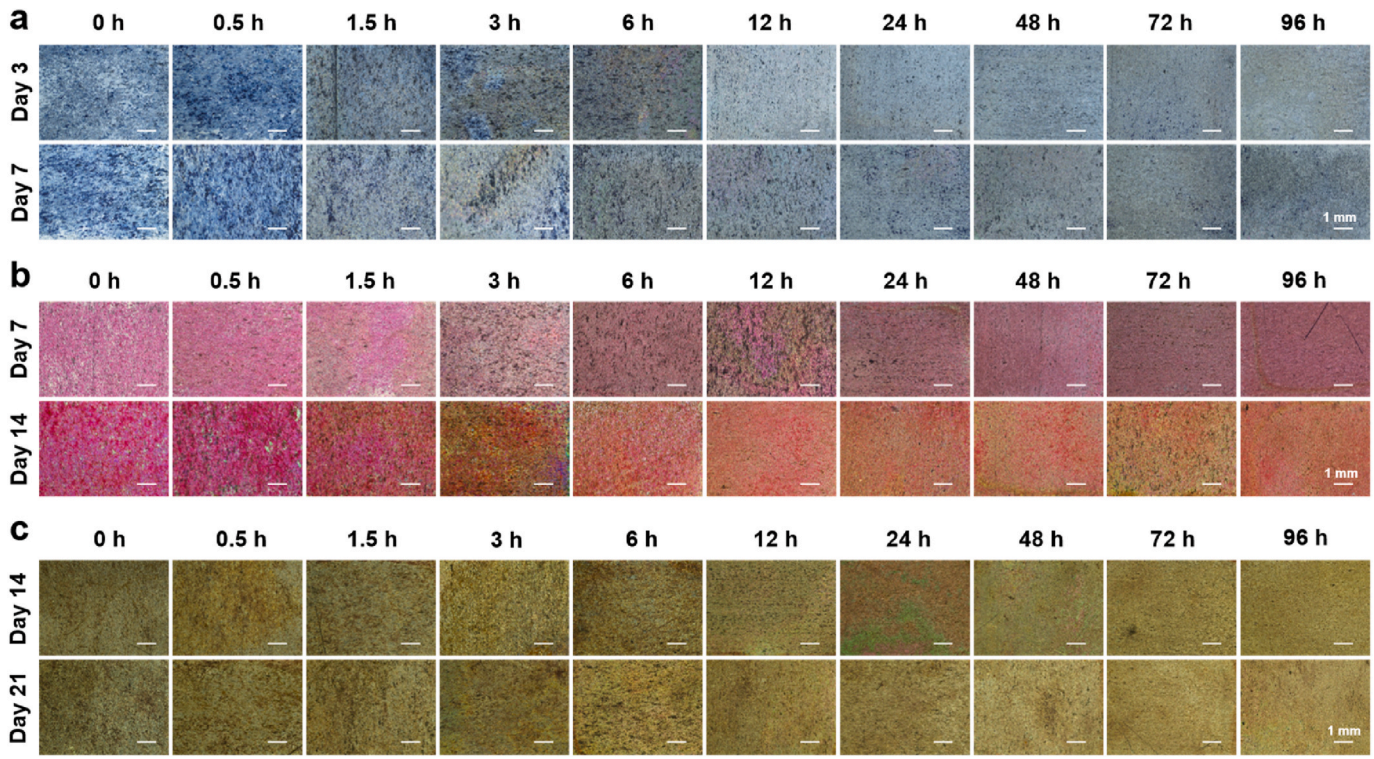

Fig. 6. Osteogenic differentiation of BMSCs cultured on the gradient coating. (a) Optical images of ALP activity of BMSCs after osteogenic induction for 3 and 7 days. (b) Optical images of collagen type I secreted by BMSCs after osteogenic induction for 7 and 14 days. (c) Optical images of mineralization nodule of BMSCs after osteogenic induction for 14 and 21 days.

signaling pathways. The genes involved in these pathways were further clustered to investigate the interactions at the protein level (Fig. 9g and h). Adequate links of upregulated DEGs in protein-protein interaction (PPI) networks were directed into mini-chromosome maintenance complex component 7 (Mcm7), cell division cycle 5 (Cdca5) and Brca1, while the downregulated DEGs were enriched into TNF, NF-κB, Ccl4, Cxcl3 and IL-1β. The protein encodes by Mcm is one of the highly conserved mini-chromosome maintenance proteins family that is essential for the initiation of eukaryotic genome replication, cell proliferation and migration [46]. Cdca5 and Brca1 are essential in DNA repair and recombination. As typical inflammatory cytokines, Ccl4 and Cxcl3 can be generated by MΦs through the NF-κB signaling pathway [47]. IL-1β is also an inflammatory factor secreted by MΦs.

The bioinformatic analysis of DEGs in TA-0.5 *vs* TA-48 was performed to investigate the immune responses of MΦs cultured on large-sized and small-sized nanowires. Go term enrichment analysis displayed that the upregulated DEGs were concentrated in MyD88-dependent Toll-like receptor signaling pathway, immune system process, cytoplasm, MΦ colony-stimulating factor receptor binding, while the downregulated DEGs were enriched in ATP metabolic process, cytoplasmic translation and positive regulation of intrinsic apoptotic signaling pathway by p53 class mediator (Figs. S7c and f). The upregulated genes were mainly enriched in NF-κB, Toll-like receptor, TNF, and p53 signaling pathways, while the downregulated genes were focused on ribosome, focal adhesion, and PI3K-Akt signaling pathways (Fig. 9j). The abundance links of upregulated DEGs in PPI networks (Fig. 9k and l) were directed to Src, IL-6, Mmp9, and Ccl5, while the downregulated DEGs were directed to the Rpl19, Rps18 and Rps7. Integrins are involved in cell adhesion, podosome formation, and MΦ activation [48–50]. Upregulation of the integrin-binding gene Src increases cytoskeletal contractility, which can be detrimental to podosome formation [48]. Higher cellular elastic modulus is associated with M1-type MΦ activation. Therefore, upregulation of Src may lead to a pro-inflammatory response in TA-48. IL-6 is a typical proinflammatory factor that triggers the immune response [51]. The upregulation of IL-6 in TA-48 further exacerbated the inflammatory response.

3.7. *In vivo* osseointegration ability of the implants with the screened nanowire coatings

In vitro data revealed that the TA-0.5 group could manipulate a favorable immunomodulatory microenvironment and directly promote osteogenesis and angiogenesis when compared with T and TA-48 groups. *In vivo* experiments were performed to confirm the *in vitro* observations. The X-ray images of the implants and surrounding bone tissue (Fig. 10a) showed that the implants were successfully implanted into the bone defect sites. The results of protein expression levels around the implants are shown in Fig. 10b. On the 3rd day, the expression levels of iNOS and IL-1β in the three groups have no obvious difference. Anti-inflammation-associated proteins CD206 and Arg1 both showed low levels. While on the 7th day, the TA-0.5 group showed a significant down-regulation of inflammation-associated proteins, whereas inflammation failed to resolve in the T and TA-48 groups. As for the anti-inflammatory proteins such as CD206 and Arg1, TA-0.5 had an obvious enhancement on the 7th day than the 3rd day. However, no significant changes can be seen in the T and TA-48 groups. Furthermore, TA-0.5 could induce higher expression levels of angiogenic (Ang1 and CD31) and osteogenic (OPN and ALP) related proteins when compared with other two groups.

In the 6th week, 3D-reconstructed micro-CT images confirm the results. It displayed that abundant new bone (in yellow) was synthesized around TA-0.5 compared with other groups (Fig. 10c). The quantitative data also confirmed the results. BV/TV, Tb. Th, and Tb. N of TA were 44.6 %, 0.055 mm, and 9.79 mm^{-1}, respectively, all of which were significantly higher than those of other groups. The Tb. Sp of TA-0.5 group was 0.045 mm, which was lower than T and TA-48 groups. The quantitative data in Fig. S10 and Fig. S11 displayed the new bone formation ability. The histological staining showed there was more new

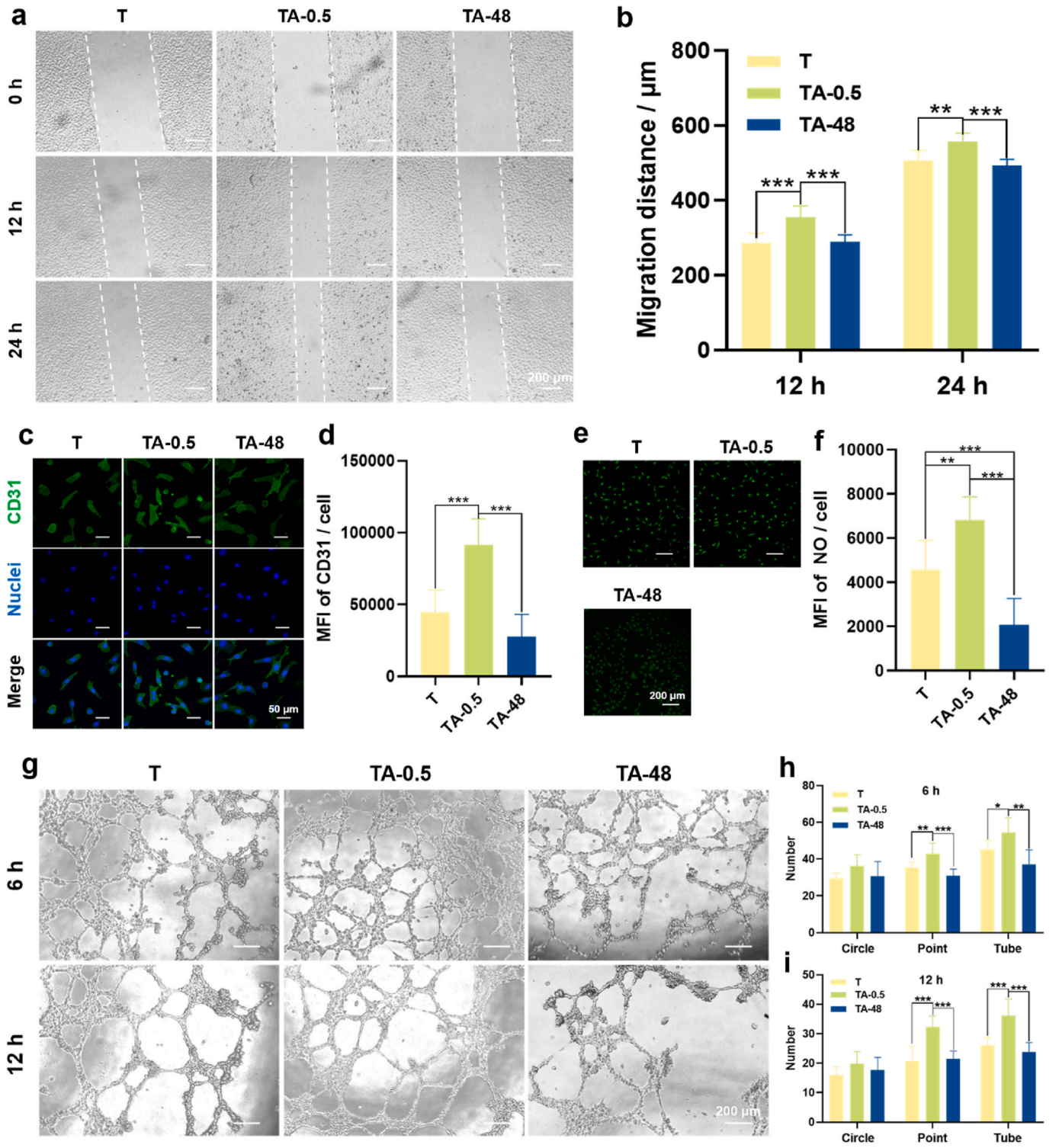

Fig. 7. Effects of the conditioned DMEM of MΦs on angiogenesis of ECs. (a) Optical images of EC migration after incubation with the conditioned DMEM for 0, 12, and 24 h. (b) Migration distance of the ECs. (c) Fluorescence images of CD31 of ECs after incubated in the conditioned DMEM for 24 h. (d) Quantitative results of the CD31. (e) Fluorescence images of NO of ECs after incubated in the conditioned DMEM for 24 h. (f) Quantitative result of the NO. (g) Optical images of ECs incubated in the conditioned DMEM on the ECMatrix™ gel for 6 and 12 h. (h) Quantitative statistics for structural components (circles, points and tubes) of vascular networks after 6 h of incubation. (i) Quantitative statistics for structural components (circles, points and tubes) of vascular networks after 12 h of incubation. $^{*}p < 0.05$, $^{**}p < 0.01$, and $^{***}p < 0.001$ using one-way ANOVA with a Tukey post hoc test.

bone tissue (in blue) contact with the surface of the implant (Fig. 10d). Collectively, the TA-0.5 group was deemed to markedly facilitated *de novo* bone formation *in vivo*, which is consistent with the *in vitro* results.

4. Discussion

Constructing nanostructured coating on Ti implant surfaces is considered to be an effective strategy to enhance implant

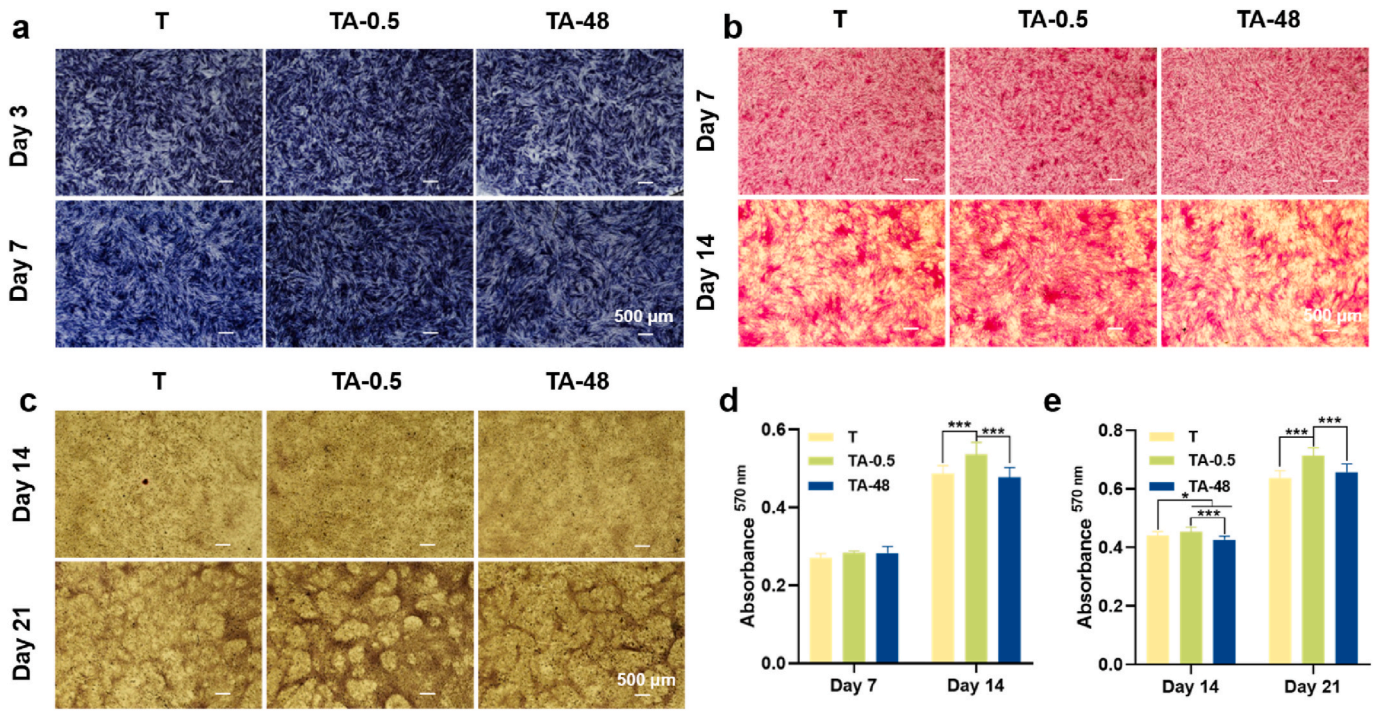

Fig. 8. Effects of the conditioned α-MEM of MΦs on osteogenic differentiation of BMSCs. (a) Optical images of ALP activity of BMSCs after osteogenic induction for 3 and 7 days. (b) Optical images of type I collagen secreted by BMSCs after osteogenic induction for 7 and 14 days. (c) Optical images of mineralization nodule of BMSCs after osteogenic induction for 14 and 21 days. (d) Quantitative of type I collagen. (e) Quantitative of ECM mineralization. $^{*}p < 0.05$, $^{**}p < 0.01$ and $^{***}p < 0.001$ using one-way ANOVA with a Tukey post hoc test.

osseointegration [8]. Nanowires among them are ideal nanostructures due to their ability to mimic the nanoscale collagen fibers of the host bone [52,53]. Our previous study demonstrated that highly porous nanofibers downregulate inflammation-related signaling pathways, thereby accelerating osseointegration during the early stages of fracture healing [16]. Additionally, nanotube diameter plays a critical role in influencing osseointegration. TiO_2 nanotubes with a diameter of 15 nm, compared to those with diameters of 60 nm and 120 nm, significantly enhanced macrophage polarization toward M2 phenotype, creating a favorable immune microenvironment for early osseointegration [10,54].

Compared with traditionally time-consuming and costly orthogonal experiments, high-throughput screening of nano-morphology on Ti implant surfaces has emerged as a potent approach for elucidating cell-material interactions, leveraging its systematic, efficient, precise, and scalable benefits [55–57]. Here, we introduced a temporal microdroplet technique for fabricating gradient coating with continuous nanowire size on Ti surfaces using a one-step alkaline etching method. With the controlled preparation of the gradient coating, the nanowire size with optimal osseointegration ability was effectively screened following cell culture on the coating surface. The limitation posed by discontinuous preparation parameters on Ti implant surfaces was alleviated by enhancing throughput and substantially reducing errors associated with inter-sample variation, thereby significantly saving time and costs. This preparation technique of gradient coating and high-throughput screening method not only offer a new paradigm for exploring biomaterials, but also establish a foundation for multidisciplinary material design and development.

Synchronized validation of multicellular functionality on the material surfaces is crucial. Osseointegration is a complex process involving various cells, mainly including MΦs, ECs, and BMSCs [5]. It's notable that osteoimmunomodulation, garnering considerable attention in recent years, is pivotal in the early stage of osseointegration, during which process MΦs play a key role [30]. ECs are the cells that underlie angiogenesis, and new blood vessels transport oxygen, nutrients, and cytokines needed during osteogenesis. In the process of osseointegration, BMSCs are recruited to the injury site and subsequently undergo differentiation into new osteoblasts, facilitating bone regeneration [58]. It was shown that nanowires with small dimensions promoted M2 polarization of MΦs, while that of large dimensions exhibited opposite trend. The schematic illustration of the key signal transduction cascades of MΦs affected by TA-0.5 in comparison with T and TA-48 is shown in Fig. 9m. TA-0.5 elevated the expression levels of FAK, RhoGEF, ROCK, and MLC (Fig. S8), promoting ECM assembly, integrin activation, and pedunculated synapse formation in MΦs [59]. Simultaneously, this process activated the PI3K-Akt signaling pathway, stimulating the secretion of growth factors including TGF-β, Brca1, Cdk4, Ccnb1, and Ccnb2 [60]. The activated PI3K-Akt signaling pathway concurrently inhibited the NF-κB signaling pathway and decreased the production of inflammatory cytokines [61]. CD14 and TLR-4 were markedly down-regulated in the TA group (Fig. S9), resulting in TLR signaling pathway attenuation. Moreover, attenuation of the TLR, IL-1β, and TNF signaling pathways in the TA-0.5 group ultimately intersected with the downstream of NF-κB signaling cascade, leading to decreased transcription of pro-inflammatory factors such as IKB-α, CXCL, LIF, MIP-1β, MCP-1, A20, and CCL (Fig. S9). ECs and BMSCs may be regulated by the nanowire coatings with the similar mechanisms. Collectively, the coating with small nanowire size could promote M2 polarization of MΦs, angiogenesis of ECs, and osteogenic differentiation of BMSCs both *in vitro* and *in vivo*.

The method developed to fabricate gradient nanowire coating in the present work is not only suitable for Ti implants, but can also be referenced for other metallic biomaterials. For example, our previous work showed that nanosheet coatings could be grown on nearly equiatomic nickel-titanium (NiTi) alloy in NaOH solution [62]. Using the method developed, gradient nanosheet coatings may be fabricated on the NiTi alloy. Although the solution used in the present work was alkaline solution, other solutions such as acid and neutral solutions can also be used to fabricate a variety of surface gradient structures. Additionally, the method can combine with other methods such as anodization, micro-arc

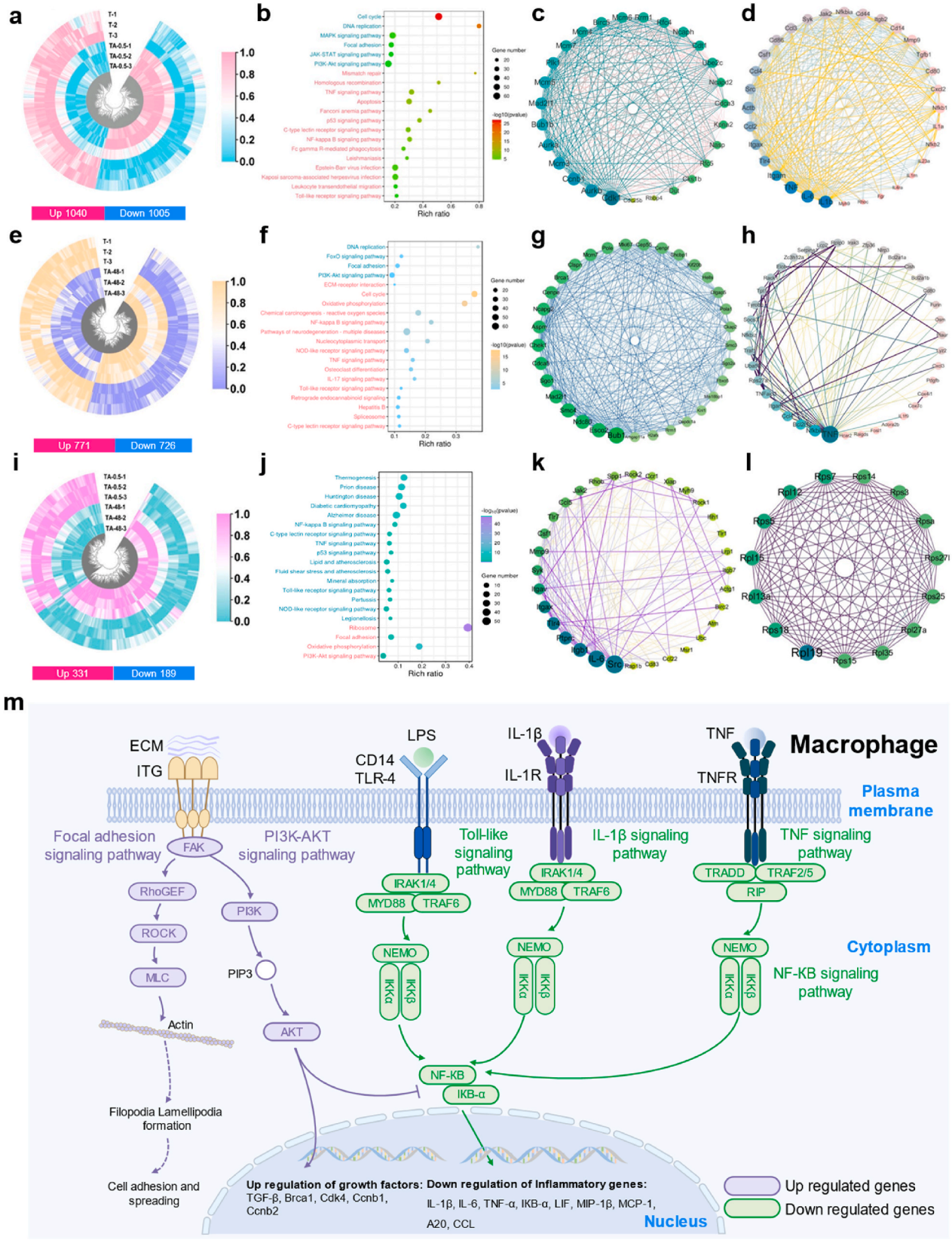

Fig. 9. mRNA sequence analysis of MΦs cultured on selected surfaces. (a) Heatmap of the DEGs of T *vs* TA-0.5. (b) Top 20 of KEGG enrichment analysis of T *vs* TA-0.5. (c–d) Upregulated/downregulated protein interactions analysis of T *vs* TA-0.5. (e) Heatmap of the DEGs of T *vs* TA-48. (f) Top 20 of KEGG enrichment analysis of T *vs* TA-0.5. (g–h) Upregulated/downregulated protein interactions analysis of T *vs* TA-0.5. (i) Heatmap of the DEGs of TA-0.5 *vs* TA-48. (j) Top 20 of KEGG enrichment analysis of TA-0.5 *vs* TA-48. (k–l) Upregulated/downregulated protein interactions analysis of TA-0.5 *vs* TA-48. (m) Schematic illustration of the key signal transduction cascades of MΦs affected by TA-0.5 in comparison with T and TA-48.

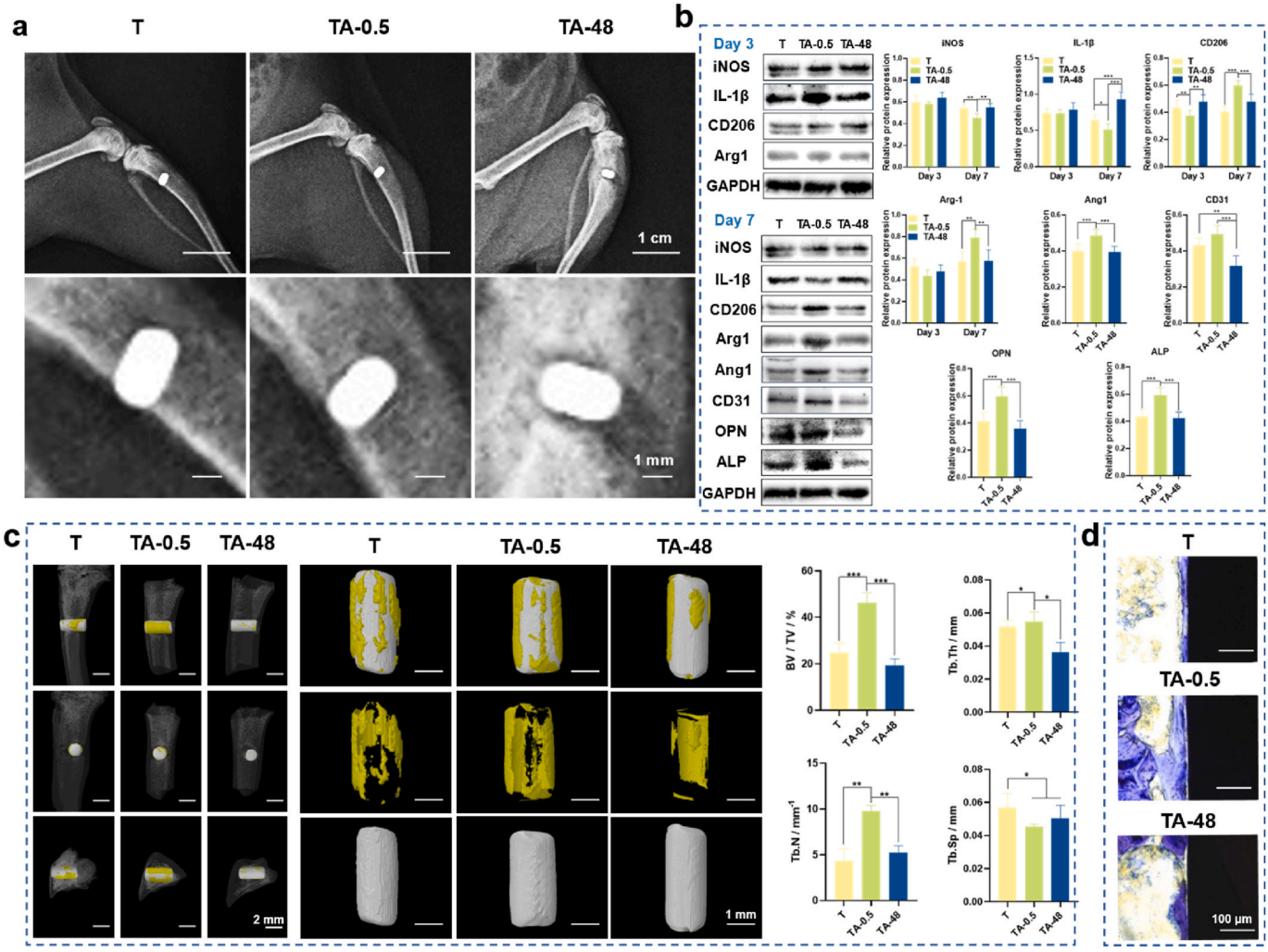

Fig. 10. *In vivo* osteoimmunology and osseointegration ability of the implants. (a) X-ray images of the implants and bone. (b) Western blot results of peri-implant tissues after 3 and 7 days of implantation. (c) 3D Micro-CT images of the implants and the peri-implant bone tissue and quantified parameters of microstructures (BV/TV, Tb.Th, Tb.N, and Tb.Sp). (d) Histological staining of peri-implant bone tissue by toluidine blue. $^{*}p < 0.05$, $^{**}p < 0.01$, and $^{***}p < 0.001$ using one-way ANOVA with a Tukey post hoc test.

oxidation, hydrothermal treatment, electrodeposition, and electrophoretic deposition to extend its applicability. Some of the works are ongoing in our laboratory and additional findings will be reported in due course.

5. Conclusion

Gradient nanowire coatings were fabricated on Ti surfaces using a one-step alkaline etching method. The average nanowire diameter and inter-spacing continuously increased from 8.7 nm to 43.2 nm for 0.5 h of etching to 37.7 nm and 386.2 nm for 96 h of etching, respectively. Small-sized nanowires that the diameter is 5.63–14.25 nm and the inter-spacing is 29.42–57.97 nm were found to polarize MΦs towards M2 phenotype through downregulating inflammation-related signaling pathways, which is beneficial for subsequent angiogenesis and osteogenesis. In addition, the small-sized nanowires could also directly promote angiogenesis of ECs and osteogenic differentiation of BMSCs. Animal experiments showed that small-sized nanowires could timely polarized MΦs to M2 phenotype, upregulated the expression of angiogenic and osteogenic proteins, finally ameliorated osseointegration compared with that of large-sized ones, well corroborating the *in vitro* observations. In addition to gradient alkali etching coatings, other gradient coatings may also be produced based on the method developed in the present work, which is significantly meaningful for efficient and cost-effective design and preparation of surface coatings of advanced biomaterials.

CRediT authorship contribution statement

Ruiyue Hang: Writing – original draft, Visualization, Validation, Methodology, Investigation, Formal analysis, Data curation, Conceptualization. **Yuyu Zhao:** Validation, Software, Resources, Methodology, Data curation. **Huanming Chen:** Validation, Software, Methodology, Data curation. **Xiaomei Li:** Validation, Software, Investigation, Data curation. **Runhua Yao:** Validation, Software, Investigation, Data curation. **Yonghua Sun:** Validation, Software, Investigation, Data curation. **Xiaohong Yao:** Writing – review & editing, Supervision, Project administration, Funding acquisition, Conceptualization. **Long Bai:** Writing – review & editing, Supervision, Software, Resources, Methodology, Conceptualization. **Huaiyu Wang:** Validation, Supervision, Software, Methodology, Conceptualization. **Yong Han:** Writing – review & editing, Supervision, Project administration, Methodology, Funding acquisition, Conceptualization. **Ruiqiang Hang:** Writing – review & editing, Supervision, Project administration, Methodology, Funding acquisition, Conceptualization.

Declaration of competing interest

The authors declare that they have no known competing financial interests or personal relationships that could have appeared to influence the work reported in this paper.

Acknowledgements

This work was jointly supported by State Key Laboratory for Mechanical Behavior of Materials (20232503), the Four "Batches" Innovation Project of Invigorating Medical through Science and Technology of Shanxi Province (2022XM12), the Key Research and Development Program of Shanxi Province (202102130501007), and the Natural Science Foundation of Shanxi Province (202203021211173).

Appendix A. Supplementary data

Supplementary data to this article can be found online at https://doi.org/10.1016/j.mtbio.2024.101392.

Data availability

Data will be made available on request.

References

[1] R.J. Ferguson, A.J.R. Palmer, A. Taylor, M.L. Porter, H. Malchau, S. Glyn-Jones, Lancet 392 (2018) 1662–1671.
[2] A.J. Price, A. Alvand, A. Troelsen, J.N. Katz, G. Hooper, A. Gray, A. Carr, D. Beard, Lancet 392 (2018) 1672–1682.
[3] M. Geetha, A.K. Singh, R. Asokamani, A.K. Gogia, Prog. Mater. Sci. 54 (2009) 397–425.
[4] Y.-T. Sul, Biomaterials 24 (2003) 3893–3907.
[5] Y. Wang, Y. Zhang, R.J. Miron, Clinical Implant Dentistry and Related Research, vol. 18, 2016, pp. 618–634.
[6] X. Liu, P.K. Chu, C. Ding, Mater. Sci. Eng. R Rep. 47 (2004) 49–121.
[7] L. Zhao, H. Wang, K. Huo, L. Cui, W. Zhang, H. Ni, Y. Zhang, Z. Wu, P.K. Chu, Biomaterials 32 (2011) 5706–5716.
[8] M. Eskandani, H. Derakhshankhah, R. Jahanban-Esfahlan, M. Jaymand, Int. J. Biol. Macromol. 249 (2023) 125991.
[9] X. Liu, P.K. Chu, C. Ding, Mater. Sci. Eng. R Rep. 70 (2010) 275–302.
[10] L. Bai, Y. Zhao, P. Chen, X. Zhang, X. Huang, Z. Du, R. Crawford, X. Yao, B. Tang, R. Hang, Y. Xiao, Small 17 (2020) 2006287.
[11] M. Yu, H. Yang, B. Li, R. Wang, Y. Han, Chem. Eng. J. 454 (2023) 140141.
[12] D. Yu, S. Guo, D. Yang, B. Li, Z. Guo, Y. Han, Chem. Eng. J. 426 (2021) 131187.
[13] L. Yang, S. Pijuan-Galito, H.S. Rho, A.S. Vasilevich, A.D. Eren, L. Ge, P. Habibović, M.R. Alexander, J. De Boer, A. Carlier, P. Van Rijn, Q. Zhou, Chem. Rev. 121 (2021) 4561–4677.
[14] Z. Fang, J. Chen, Y. Zhu, G. Hu, H. Xin, K. Guo, Q. Li, L. Xie, L. Wang, X. Shi, Y. Wang, C. Mao, Nat. Commun. 12 (2021) 3757.
[15] H.V. Unadkat, M. Hulsman, K. Cornelissen, B.J. Papenburg, R.K. Truckenmüller, A. E. Carpenter, M. Wessling, G.F. Post, M. Uetz, M.J.T. Reinders, D. Stamatialis, C. A. Van Blitterswijk, J. De Boer, in: Proceedings of the National Academy of Sciences, vol. 108, 2011, pp. 16565–16570.
[16] L. Bai, P. Chen, Y. Zhao, R. Hang, X. Yao, B. Tang, C. Liu, Y. Xiao, R. Hang, Biomaterials 278 (2021) 121162.
[17] Y. Zhu, H. Liang, X. Liu, J. Wu, C. Yang, T.M. Wong, K.Y. Kwan, K.M. Cheung, S. Wu, K.W. Yeung, Sci. Adv. 7 (2021) eabf6654.
[18] T. N. Golden, A. Venosa,A. J. Gow, 12 (2022).
[19] M.J. Feito, R. Diez-Orejas, M. Cicuéndez, L. Casarrubios, J.M. Rojo, M.T. Portolés, Colloids Surf., B 176 (2019) 96–105.
[20] L. Bai, Y. Liu, Z. Du, Z. Weng, W. Yao, X. Zhang, X. Huang, X. Yao, R. Crawford, R. Hang, D. Huang, B. Tang, Y. Xiao, Acta Biomater. 76 (2018) 344–358.
[21] X. Zhang, J. Shi, S. Chen, Y. Dong, L. Zhang, A.C. Midgley, D. Kong, S. Wang, Regen. Med. 14 (2019) 1089–1105.
[22] G. Caligiuri, Cardiovasc. Res. 115 (2019) 1425–1434.
[23] K. Komatsu, T. Matsuura, T. Suzumura, T. Ogawa, Materials today, Bio 23 (2023) 100852.
[24] L. Bacakova, E. Filova, M. Parizek, T. Ruml, V. Svorcik, Biotechnol. Adv. 29 (2011) 739–767.
[25] J. Pajarinen, T. Lin, E. Gibon, Y. Kohno, M. Maruyama, K. Nathan, L. Lu, Z. Yao, S. B. Goodman, Biomaterials 196 (2019) 80–89.
[26] F. Belema-Bedada, S. Uchida, A. Martire, S. Kostin, T. Braun, Cell Stem Cell 2 (2008) 566–575.
[27] A. Mantovani, A. Sica, S. Sozzani, P. Allavena, A. Vecchi, M. Locati, Trends Immunol. 25 (2004) 677–686.
[28] T. Kitaori, H. Ito, E.M. Schwarz, R. Tsutsumi, H. Yoshitomi, S. Oishi, M. Nakano, N. Fujii, T. Nagasawa, T. Nakamura, Arthritis Rheum. 60 (2009) 813–823.
[29] F. Zhao, B. Lei, X. Li, Y. Mo, R. Wang, D. Chen, X. Chen, Biomaterials 178 (2018) 36–47.
[30] Z. Chen, T. Klein, R.Z. Murray, R. Crawford, J. Chang, C. Wu, Y. Xiao, Mater. Today 19 (2016) 304–321.
[31] E. Wei, M. Hu, L. Wu, X. Pan, Q. Zhu, H. Liu, Y. Liu, Stem Cell Res. Ther. 15 (2024) 156.
[32] J. Wei, J. Shimazu, Munevver p. Makinistoglu, A. Maurizi, D. Kajimura, H. Zong, T. Takarada, T. Iezaki, Jeffrey e. Pessin, E. Hinoi, G. Karsenty, Cell 161 (2015) 1576–1591.
[33] B. A. Byers,A. J. García, 10 (2004) 1623-1632.
[34] W.G. Jang, E.J. Kim, I.-H. Bae, K.-N. Lee, Y.D. Kim, D.-K. Kim, S.-H. Kim, C.-H. Lee, R.T. Franceschi, H.-S. Choi, J.-T. Koh, Bone 48 (2011) 885–893.
[35] W. Michowski, J.M. Chick, C. Chu, A. Kolodziejczyk, Y. Wang, J.M. Suski, B. Abraham, L. Anders, D. Day, L.M. Dunkl, M. Li Cheong Man, T. Zhang, P. Laphanuwat, N.A. Bacon, L. Liu, A. Fassl, S. Sharma, T. Otto, E. Jecrois, R. Han, K.E. Sweeney, S. Marro, M. Wernig, Y. Geng, A. Moses, C. Li, S.P. Gygi, R.A. Young, P. Sicinski, Mol. Cell 78 (2020) 459–476.e413.
[36] O. Gavet, J. Pines, Dev. Cell 18 (2010) 533–543.
[37] A. Parrilla, L. Cirillo, Y. Thomas, M. Gotta, L. Pintard, A. Santamaria, Cell Cycle 15 (2016) 3177–3182.
[38] L. Liu, T. Tao, S. Liu, X. Yang, X. Chen, J. Liang, R. Hong, W. Wang, Y. Yang, X. Li, Y. Zhang, Q. Li, S. Liang, H. Yu, Y. Wu, X. Guo, Y. Lai, X. Ding, H. Guan, J. Wu, X. Zhu, J. Yuan, J. Li, S. Su, M. Li, X. Cai, J. Cai, H. Tian, Nat. Commun. 12 (2021) 2693.
[39] A. Oberholzer, C. Oberholzer, L.L. Moldawer, Crit. Care Med. 28 (2000).
[40] T. Sparre, U. Bjerre Christensen, C.F. Gotfredsen, P. Mose Larsen, S.J. Fey, K. Hjernø, P. Roepstorff, F. Pociot, A.E. Karlsen, J. Nerup, Diabetologia 47 (2004) 892–908.
[41] R. Zhao, H. Zhou, S.B. Su, Int. Immunopharm. 17 (2013) 658–669.
[42] J. Mudter, M.F. Neurath, Inflamm. Bowel Dis. 13 (2007) 1016–1023.
[43] J.J. Leija-Martínez, B.E. Del-Río-Navarro, F. Sanchéz-Muñoz, O. Muñoz-Hernández, E. Hong, A. Giacoman-Martínez, R. Romero-Nava, K.L. Patricio-Román, M.S. Hall-Mondragon, D. Espinosa-Velazquez, S. Villafaña, F. Huang, Clin. Immunol. 229 (2021) 108715.
[44] G.V. Halade, Y.-F. Jin, M.L. Lindsey, Pharmacol. Ther. 139 (2013) 32–40.
[45] K. Krause, R. Sabat, E. Witte-Händel, A. Schulze, V. Puhl, M. Maurer, K. Wolk, Br. J. Dermatol. 180 (2019) 859–868.
[46] M. Pacek, J.C. Walter, EMBO J. 23 (2004) 3667–3676.
[47] A.N. Edris, E.B. Aboulhoda, S.S. El-Din, M.A. Fouad, E. Albadawi, A.L. Rashed, B. K. Elessawy, Combinatorial Chemistry & High Throughput Screening, vol. 26, 2023, pp. 489–497.
[48] P. Friedl, B.J.N.I. Weigelin, Nat. Immunol. 9 (2008) 960–969.
[49] L.T. Duong, G.a.J.C. M. Rodan, T. Cytoskeleton, Cell Motility and the Cytoskeleton, vol. 47, 2000, pp. 174–188.
[50] L. Lv, Y. Xie, K. Li, T. Hu, X. Lu, Y. Cao, X.J.a.H.M. Zheng, Adv. Healthcare Mater. 7 (2018) 1800675.
[51] P. Baran, S. Hansen, G.H. Waetzig, M. Akbarzadeh, L. Lamertz, H.J. Huber, M. R. Ahmadian, J.M. Moll, J. Scheller, J. Biol. Chem. 293 (2018) 6762–6775.
[52] Y. Zhang, Z. Li, H. Guo, Q. Wang, B. Guo, X. Jiang, Y. Liu, S. Cui, Z. Wu, M. Yu, L. Zhu, L. Chen, N. Du, D. Luo, Y. Lin, P. Di, Y. Liu, Adv. Sci. 11 (2024) 2310292.
[53] W.-Q. Zhu, S.-Y. Shao, L.-N. Xu, W.-Q. Chen, X.-Y. Yu, K.-M. Tang, Z.-H. Tang, F.-M. Zhang, J. Qiu, J. Nanobiotechnol. 17 (2019) 55.
[54] Q.L. Ma, L.Z. Zhao, R.R. Liu, B.Q. Jin, W. Song, Y. Wang, Y.S. Zhang, L.H. Chen, Y. M. Zhang, Biomaterials 35 (2014) 9853–9867.
[55] T.G. Fernandes, M.M. Diogo, D.S. Clark, J.S. Dordick, J.M. Cabral, Trends Biotechnol. 27 (2009) 342–349.
[56] J. Seo, J.-Y. Shin, J. Leijten, O. Jeon, G. Camci-Unal, A.D. Dikina, K. Brinegar, A. M. Ghaemmaghami, E. Alsberg, A. Khademhosseini, Biomaterials 153 (2018) 85–101.
[57] Y. Li, S. Wang, Y. Dong, P. Mu, Y. Yang, X. Liu, C. Lin, Q. Huang, Bioact. Mater. 5 (2020) 1062–1070.
[58] F.-M. Chen, L.-A. Wu, M. Zhang, R. Zhang, H.-H. Sun, Biomaterials 32 (2011) 3189–3209.
[59] J.M. Kalappurakkal, A.A. Anilkumar, C. Patra, T.S. Van Zanten, M.P. Sheetz, S. Mayor, Cell 177 (2019) 1738–1756.e1723.
[60] G. Song, G. Ouyang, S. Bao, J. Cell Mol. Med. 9 (2005) 59–71.
[61] H. Qi, M. Shi, Y. Ni, W. Mo, P. Zhang, S. Jiang, Y. Zhang, X. Deng, Adv. Healthcare Mater. 10 (2021) 2100994.
[62] Y. Zhao, L. Bai, Y. Sun, X. Yao, X. Huang, R. Hang, D. Huang, Corrosion Sci. 190 (2021) 109654.